

Titre: Digital image analysis for strain measurements
Title:

Auteur: Harald Kanduth
Author:

Date: 1998

Type: Mémoire ou thèse / Dissertation or Thesis

Référence: Kanduth, H. (1998). Digital image analysis for strain measurements [Mémoire de maîtrise, École Polytechnique de Montréal]. PolyPublie.
Citation: <https://publications.polymtl.ca/6904/>

 **Document en libre accès dans PolyPublie**
Open Access document in PolyPublie

URL de PolyPublie: <https://publications.polymtl.ca/6904/>
PolyPublie URL:

**Directeurs de
recherche:** Robert Corthésy
Advisors:

Programme: Non spécifié
Program:

UNIVERSITÉ DE MONTRÉAL

**DIGITAL IMAGE ANALYSIS
FOR STRAIN MEASUREMENTS**

**HARALD KANDUTH
DÉPARTEMENT DES GÉNIES CIVIL, GÉOLOGIQUE ET DES MINES
ÉCOLE POLYTECHNIQUE DE MONTRÉAL**

**MÉMOIRE PRÉSENTÉ EN VUE DE L'OBTENTION
DU DIPLÔME DE MAÎTRISE ÈS SCIENCES APPLIQUÉES
(GÉNIE MINÉRAL)
OCTOBRE 1998**

© Harald Kanduth, 1998.



National Library
of Canada

Acquisitions and
Bibliographic Services

395 Wellington Street
Ottawa ON K1A 0N4
Canada

Bibliothèque nationale
du Canada

Acquisitions et
services bibliographiques

395, rue Wellington
Ottawa ON K1A 0N4
Canada

Your file Votre référence

Our file Notre référence

The author has granted a non-exclusive licence allowing the National Library of Canada to reproduce, loan, distribute or sell copies of this thesis in microform, paper or electronic formats.

The author retains ownership of the copyright in this thesis. Neither the thesis nor substantial extracts from it may be printed or otherwise reproduced without the author's permission.

L'auteur a accordé une licence non exclusive permettant à la Bibliothèque nationale du Canada de reproduire, prêter, distribuer ou vendre des copies de cette thèse sous la forme de microfiche/film, de reproduction sur papier ou sur format électronique.

L'auteur conserve la propriété du droit d'auteur qui protège cette thèse. Ni la thèse ni des extraits substantiels de celle-ci ne doivent être imprimés ou autrement reproduits sans son autorisation.

0-612-38685-6

Canada

UNIVERSITÉ DE MONTRÉAL

ÉCOLE POLYTECHNIQUE DE MONTRÉAL

Ce mémoire intitulé:

**DIGITAL IMAGE ANALYSIS
FOR STRAIN MEASUREMENTS**

présenté par: KANDUTH Harald

en vue de l'obtention du diplôme de: Maîtrise ès sciences appliquées

a été dûment accepté par le jury d'examen constitué de:

M. GILL Denis E., Ph.D., président

M. CORTHÉSY Robert, Ph.D., membre et directeur de recherche

M. DEEP George, Ph.D., membre

REMERCIEMENTS

Au terme de cette étude, je tiens tout d'abord à exprimer ma profonde reconnaissance à Dr. Robert Corthésy qui par sa rigueur et sa disponibilité m'a permis de mener à bien mes recherches.

J'exprime également mes plus sincères remerciements aux personnes suivantes:

Michel Cantin et Alain Coulombe, Solvision Inc, Claude Avrilleau, D.A.Usinage et Denis Jacob, Centre de Technologie Noranda pour leur assistance pendant la conception de la méthode et la construction de l'appareil expérimental.

Je remercie chaleureusement la direction du Département de Mines et Exploration du Centre de Technologie Noranda qui m'avait accordé l'appui pour l'exécution de cette recherche.

RÉSUMÉ

Un concept optique de signaux numériques pour mesurer des micro-déformations a été développé. Ce concept offre la possibilité d'égaliser ou de surpasser la précision et l'exactitude obtenues avec les méthodes traditionnelles de mesure de contraintes. Cette nouvelle méthode élimine la nécessité de mettre en contact le capteur avec la surface à mesurer, supprimant ainsi les problèmes associés au contact du capteur avec la surface.

Le principe opérationnel du capteur optique consiste en la création d'images photographiques numériques de la surface dont la déformation doit être mesurée avant et après l'application de la contrainte. Les images sont séparées l'une de l'autre par une distance connue et constante. Elles sont sauvegardées en fichiers graphiques dans un ordinateur, puis analysées. L'analyse consiste à déterminer le changement de la distance entre les zones présélectionnées sur des images par un procédé appelé « appariement modèle-objet ». La valeur de la contrainte provient de la division de la différence dérivée en distance (Δ) par la longueur totale de la jauge de déformation (L , la distance entre les images).

Afin de valider la viabilité du nouveau concept, un appareil expérimental a été construit dans le but de comparer les mesures de déformations obtenues par celui-ci avec celles des jauges électriques courantes en utilisant des éprouvettes prélevées sur différents matériaux et soumises à des essais de compression uniaxiale.

De façon générale, les séries d'essais ont réussi à démontrer la viabilité du concept de capteur de déformation optique numérique. Des écarts se sont produits dans quelques-uns des résultats mais la plupart d'entre eux peuvent être attribués à certaines lacunes relatives à l'appareil expérimental, la méthode de traitement de l'image et les procédures d'essai.

Il est certain qu'un système optimisé ainsi que l'amélioration des procédures va mener à une technique offrant la possibilité d'égaliser ou de surpasser la précision et l'exactitude obtenues avec les méthodes traditionnelles de mesure de déformations, avec, cependant, un avantage significatif: cette nouvelle méthode élimine la nécessité de mettre en contact le capteur avec la surface à mesurer, supprimant ainsi les problèmes associés au contact du capteur avec la surface.

ABSTRACT

An optical-digital concept for the measurement of micro strains was developed which has the potential to match or to surpass the precision and accuracy of that of conventional strain measurement methods. The method obviates the need for contact of the sensor with the surface to be measured, thus eliminating problems associated with contact of the sensor with the surface.

The operating principle of the optical sensor is the creation of digital photographic images of the surface whose strain is to be measured before and after strain is induced. The images are separated from one another by a known, constant distance. The images are stored as graphic files in a computer and are analyzed. The analysis consists of the determination of the distance between pre-selected areas on opposing images before and after the strain was induced, and measuring the difference of the distance between these features as a result of the strain.

In order to validate the viability of the novel concept, an experimental apparatus was constructed with the purpose of comparing strain measurements with the apparatus with that of conventional electrical strain gauges, using test specimens of different materials under compressive loads. The apparatus consists of two CCD cameras in conjunction with suitable optical equipment arranged at fixed distances from one another, which permits two areas of the surface to be photographed. The images are digitized by means

of a frame grabber and are stored as .TIF files on a PC computer. The strain measurement comprises a process termed “template matching”, which involves the random selection and determination of the location of areas (templates) on the reference images before the induction of strain, searching for the same templates on the images created after the strain was induced, and determining the new locations. The strain value is derived by dividing the derived difference in distance (Δ) over the total length of the strain gauge (L , the distance between the images).

Initial tests with the apparatus were carried out to determine image size, pixel dimensions and distance between the two images. The surface illumination was optimized so as to obtain the best possible image within the limitations of the experimental apparatus. A problem with image movement was identified as the source of erratic measurements, which could be overcome by using a battery as power source for the cameras rather than an electrical line transformer.

In order to demonstrate the validity of the novel method, a series of uniaxial loading tests with instrumented test specimens of different materials was conducted to directly compare the strain measurements with the optical strain gauge to that of electrical strain gauges. The tests were designed to not only demonstrate the viability of the concept but also to simulate a rosette strain gauge and to study the effect of different surface morphologies on the capability of the sensor to measure strains.

The test samples consisted of diamond drill rock cores and a machined aluminum rod respectively, all with a diameter of 100 mm and a L/D ratio of 2.0. Electrical strain rosettes were attached on the sides of the test specimens. The test samples were loaded axially in a Tinius Olson press. The optical strain gauge was installed on the test machine table so that it was possible to photograph the specimen surface immediately next to one or between two of the rosettes at the same angles as that of the strain gauges comprising the rosettes. Measurements were done parallel, perpendicular and at 45° to the direction of the applied load.

It was found that the optical strain gauge performed very well in axial strain measurements. In tests with aluminum, granite, limestone and potash the results of the optical strain gauge were virtually identical with that of the respective electrical strain gauges. Slight differences between the strain measurements were attributed to the fact that the optical strain gauge was not measuring at the exact same location as the comparative electrical strain gauges, and that actual strains on different locations of the specimen surfaces were not identical.

The good results are especially remarkable for the test with potash and limestone, where the surface images of the former were almost devoid of features and template matching series for both materials had relatively large standard deviations. It is also noteworthy that all results were obtained in spite of the large ratio between image displacements caused by the axial translation of the test specimens in the direction of the applied loads

and the small displacements attributable to the compressional strain in the test specimen. In the experimental apparatus these translational displacements generally lead to difficulties in accurately determining the positions of the templates because of changes in lighting angles, image distortions and the movement of image features beyond the image boundaries.

In tests at 45° to the direction of the load it was found that most of the measurements with the optical sensor were to varying degrees erratic, which could be explained by the large axial translation of the test specimens relative to the small strain displacements obtained at 45° . The results show that in the test with limestone there was good correlation while in the test with aluminum the optical sensor values follow the theoretical curve much closer than either of the electrical strain gauges. Poor correlations were obtained in tests with granite and potash.

As in tests at 45° , most of the measurements with the optical sensor normal to the load were to varying degrees erratic, again attributed to the large axial translation of the test specimens relative to the small strain displacements. In spite of this, the results of the optical strain gauge measurements were very good in the tests with aluminum and limestone. In the former, the data agreed well with that of the theoretical strains and the measurements with one of the strain gauges. On the other hand there was not very good correlation in the tests with granite and potash

In general, the test series were successful in demonstrating the viability of the optical-digital strain sensor concept. There were discrepancies in some of the result, but most of these can be attributed to some of the shortcomings in the experimental apparatus, the image processing method and the test procedures. The apparatus and procedures were not designed to optimize the optical-digital method, but merely to demonstrate the principle and to identify some of the characteristics of the method. In that, the test series has very well succeeded and has met its objectives.

It is certain that an optimized system with coaxial lighting, more suitable optical equipment and a more suitable camera system (such as the use of a high capacity single camera, for example), will produce better quality images and eliminate the effect of image jitter, compression and float. Another aspect is the large translational displacement of the image features relative to the magnitude of strain displacements. This again is a characteristic of the apparatus and the test procedure which does not reflect poorly on the viability of the concept but is rather a proof that, in spite of this obstacle, the method can deliver good results. Finally, the template matching software is probably not the best method available. It is certain that research and development for the optimization of the image recognition & position determination will produce a more robust software which will be capable of producing more accurate results.

CONDENSÉ EN FRANÇAIS

Un concept optique de signaux numériques pour mesurer des micro-déformations a été développé. Ce concept offre la possibilité d'égaliser ou de surpasser la précision et l'exactitude obtenues avec les méthodes traditionnelles de mesure de déformations. Cette nouvelle méthode élimine la nécessité de mettre en contact le capteur avec la surface à mesurer, supprimant ainsi les problèmes associés au contact du capteur avec la surface.

Le principe opérationnel du capteur optique consiste en la création d'images photographiques numériques de la surface dont la déformation doit être mesurée avant et après l'application de la contrainte. Les images sont séparées l'une de l'autre par une distance connue et constante. Elles sont sauvegardées en fichiers graphiques dans un ordinateur, puis analysées. L'analyse consiste à déterminer la distance entre les zones présélectionnées sur des images opposées avant et après l'application de la contrainte et à mesurer la différence de la distance entre les caractéristiques, résultant de la contrainte.

Afin de valider la viabilité du nouveau concept, un appareil expérimental a été construit dans le but de comparer les mesures de contraintes obtenues par celui-ci avec celles des jauges électriques courantes en utilisant des éprouvettes prélevées sur différents matériaux et soumises à des compressions uniaxiales. L'appareil est composé de deux caméras à dispositif de couplage de charge installées conjointement avec un équipement optique adéquat et disposées à distance fixe l'une de l'autre, permettant ainsi de photographier deux zones d'une surface. Les images sont numérisées à l'aide d'un

saisisseur d'image et sont sauvegardées en fichiers .TIF dans un micro-ordinateur. La mesure des déformations comprend un procédé appelé « appariement modèle-objet », lequel inclut la sélection au hasard et la détermination de l'emplacement de zones (modèles) sur les images de référence avant l'application de la contrainte ainsi que la recherche des mêmes modèles sur les images créées après la mise en charge de l'éprouvette, et la détermination des nouveaux emplacements. La valeur de la déformation provient de la division de la différence dérivée en distance (Δ) par la longueur totale de la jauge de contraintes (L , la distance entre les images).

Les premiers essais effectués avec l'appareil expérimental ont servi à déterminer la grandeur de l'image, la dimension des pixels et la distance entre les deux images. L'éclairage de la surface a été optimisé afin d'obtenir la meilleure image possible à l'intérieur des limites de l'appareil. Un problème avec le mouvement de l'image a été identifié comme étant la source de mesures irrégulières. Ce problème pourrait être corrigé en utilisant une pile pour l'alimentation en énergie des caméras plutôt qu'un transformateur électrique de basse tension.

Afin de démontrer la validité de la nouvelle méthode, une série d'essais de compression uniaxiale ont été effectués sur des éprouvettes instrumentées de différents matériaux dans le but de comparer les mesures de déformations de la jauge optique directement avec celles des jauges électriques. Ces essais ont été conçus non seulement pour démontrer la viabilité du concept mais également pour simuler une jauge en rosette et étudier l'effet de

différentes morphologies de surface sur la capacité du capteur à mesurer les déformations.

Les échantillons étaient respectivement composés de carottes de roche prélevées au moyen d'une foreuse à diamant ainsi que d'une barre d'aluminium usinée de 100 mm de diamètre et de 200 mm de longueur. Les jauges électriques en rosette étaient fixées sur les côtés des éprouvettes. Les échantillons étaient chargés en direction axiale dans une presse Tinius Olson. Le capteur optique était installé sur le bâti de la presse de façon à pouvoir photographier la surface de l'éprouvette directement à côté d'une des rosettes ou entre deux rosettes et ce, suivant les mêmes orientations que les jauges des rosettes. Les mesures ont été prises parallèlement et perpendiculairement à la direction de la charge appliquée ainsi qu'à 45° .

Il a été constaté que la jauge de déformation optique a très bien fonctionné lors de la mesure des déformations axiales. Au cours des essais avec l'aluminium, le granite, le calcaire et la potasse, les résultats obtenus avec la jauge optique étaient pratiquement identiques à ceux obtenus avec les jauges électriques respectives. Les légères différences entre les mesures de contraintes ont été attribuées au fait que la jauge optique ne mesurait pas exactement au même emplacement que les jauges électriques comparatives et au fait que les déformations réelles à différents emplacements de la surface de l'éprouvette n'étaient pas identiques, à cause de l'hétérogénéité des matériaux.

Les résultats sont particulièrement remarquables avec les essais sur la potasse et le calcaire : les images de surface pour ce dernier matériau étaient presque dépourvues de caractéristiques et la série d'appariements modèle-objet pour ces deux matériaux présentaient des écarts types relativement grands. Il convient de noter que tous les résultats ont été obtenus malgré le rapport élevé entre les déplacements d'image causés par la translation axiale des éprouvettes dans la direction des charges appliquées et les faibles déplacements attribuables à la contrainte de compression dans l'éprouvette. Avec l'appareil expérimental, ces déplacements de translation ont généralement entraîné des difficultés à déterminer de façon précise le positionnement des modèles à cause des changements dans les angles d'éclairage, des distorsions de l'image et du mouvement des caractéristiques de l'image au-delà de son contour.

Lors des essais à 45° de la direction de la charge, il a été constaté que la plupart des mesures avec le capteur optique étaient plus ou moins irrégulières, ce qui s'explique par la grande translation axiale des éprouvettes par rapport aux légers déplacements dus aux déformations obtenus à 45° . Les résultats démontrent que lors de l'essai avec le calcaire, il y avait une bonne corrélation, et lors de l'essai avec l'aluminium, les valeurs du capteur optique ont suivi la courbe théorique beaucoup plus près que toutes les jauges électriques. De faibles corrélations ont été obtenues lors des essais avec le granite et la potasse.

Comme c'était le cas lors des essais à 45° , la plupart des mesures perpendiculaires à la direction de la charge avec le capteur optique étaient plus ou moins irrégulières, ce qui

s'explique de nouveau par la grande translation axiale des éprouvettes par rapport aux légers déplacements dûs aux déformations. Malgré ce fait, les résultats de mesure avec la jauge de contraintes optique ont été très bons lors des essais avec l'aluminium et le calcaire. Les données relatives au l'aluminium ont bien concordé avec les données des déformations théoriques et les mesures de l'une des jauges de déformation. Par ailleurs, il n'y avait pas une très bonne corrélation lors des essais avec le granite et la potasse.

De façon générale, les séries d'essais ont réussi à démontrer la viabilité du concept de capteur de déformation optique numérique. Des écarts se sont produits dans quelques-uns des essais mais la plupart d'entre eux peuvent être attribués à certaines lacunes relatives à l'appareil expérimental, la méthode de traitement de l'image et les procédures d'essai. L'appareil et les procédures n'ont pas été conçus pour optimiser la méthode optique numérique mais simplement pour démontrer le principe et identifier quelques-unes des caractéristiques de la méthode. Dans cette optique, les essais ont très bien réussi et ont répondu aux objectifs.

Il est certain qu'un système optimisé avec un éclairage coaxial, un équipement optique plus approprié et un système de caméra plus adéquat (tel que l'utilisation d'une caméra unique à grande résolution) produiront des images de meilleure qualité et élimineront les effets causés par l'instabilité de l'image, la compression et le sautellement. Un autre aspect à soulever est le grand déplacement de translation des caractéristiques de l'image par rapport à l'ampleur des déplacements dûs aux déformations. Ce fait est également

une particularité de l'appareil et de la procédure d'essai qui ne sont pas liées au concept proposé, et qui démontrent que malgré ces obstacles, la méthode peut donner de bons résultats. Finalement, le logiciel d'appariement modèle-objet n'est probablement pas la meilleure méthode qui existe. Il est certain que la recherche et le développement visant à optimiser la reconnaissance d'image et la détermination du positionnement générera un logiciel plus robuste qui pourra produire des résultats plus précis.

TABLE OF CONTENTS

REMERCIEMENTS	iv
RÉSUMÉ	v
ABSTRACT	vii
CONDENSÉ EN FRANÇAIS	xii
TABLE OF CONTENTS	xviii
LIST OF TABLES	xxii
LIST OF FIGURES	xxiv
LIST OF SYMBOLS	xxvi
CHAPTER 1: INTRODUCTION	1
CHAPTER 2: BACKGROUND	2
2.1 Applications	2
2.2 Review of Strain Measurement Techniques	3
2.2.1 Electrical resistance strain gauges	3
2.2.2 Electro-optical or optical strain gauges	5
2.2.3 Vibrating wire strain gauges	6
2.2.4 Laser interferometry methods for non-contact measurements of strains	6
2.2.4.1 Speckle pattern interferometry	7
2.2.4.2 Laser holography	8
2.2.5 Optical digital image analysis techniques	9
2.2.5.1 Measurement of tensile strains in Brazilian test	9
2.2.5.2 Video extensometer	11

CHAPTER 3: NOVEL OPTICAL STRAIN SENSOR	13
3.1 Operating Principle	13
3.1.1 The principle of “Template Matching”	17
3.1.2 Image acquisition	20
3.2 Experimental Apparatus	23
3.2.1 Hardware	23
3.2.2 Image and data processing hardware and software	26
3.3 Calculations	27
3.3.1 Glossary of nomenclature, symbols, terms and conventions	27
3.3.2 Strain calculations	30
3.3.3 Effect of rotation on strain gauge length	34
3.4 Characterization of Experimental Apparatus	35
3.4.1 Micrometer calibration	35
3.4.1.1 Experimental set-up	36
3.4.1.2 Test	36
3.4.2 Determination of linear pixel dimensions	38
3.4.2.1 Test procedure	38
3.4.2.2 Test results	39
3.4.2.3 Conclusion	41
3.4.3 Determination of optical strain gauge length	42
3.4.4 Summary of characteristics of the optical strain gauge	43
3.5 Effect of the Angle of Incidence of Lighting	44

3.5.1 Introduction	44
3.5.2 Determination of the effect of changes in the angle of incidence of lighting	45
3.5.3 Experimental results	47
3.5.4 Conclusions	47
3.6 Optimization of Lighting	48
3.6.1 Introduction	48
3.6.2 Tests	50
3.6.2.1 Test procedure	51
3.6.3 Results	52
3.7 Optimization of Camera Performance	54
3.7.1 Test on the effect of power supply on the performance of CCD cameras	56
3.7.2 Test results	57
3.7.3 Conclusions	60
CHAPTER 4: VALIDATION OF THE OPTICAL-DIGITAL SENSOR AS A STRAIN GAUGE	62
4.1 Introduction	62
4.2 Experimental Methodology	63
4.2.1 Test set-up and procedure	63
4.2.2 Image processing	66
4.3 Axial Strain Measurements	70
4.3.1 Aluminum	70
4.3.2 Axial strain measurements with other materials.....	72

4.4 Strain Measurements at Other Angles	76
4.4.1 Strain measurements at 45° to the applied load	77
4.4.2 Strain measurements normal to the load	82
CHAPTER 5: DISCUSSION	88
CHAPTER 6: CONCLUSION AND RECOMMENDATIONS.....	93
REFERENCES	95

LIST OF TABLES

Table 3.4.1	X-Axis Micrometer Calibration	37
Table 3.4.2.1	X-Axis Pixel Dimension Measurement	40
Table 3.4.2.2	Y-Axis Pixel Dimension Measurement	41
Table 3.4.3.1	Measurement of Distance between the Two Images of the Experimental Optical Strain Gauge	42
Table 3.4.3.2	Test Results for the Determination of the Gauge Length	43
Table 3.4.4	Summary of characteristics of the optical strain gauge	44
Table 3.5.1	Apparent Displacement of Surficial Features as Function of the Angle of Incidence of Light	47
Table 3.6.1	Apparent X-axis Displacement as a Function of Light Source	53
Table 3.6.2	X-Axis Displacement Expressed in μ -strains	54
Table 3.7.1	Effect of Power Supply on the Movement of Camera Images	57
Table 3.7.2	Effect of Power Supply on Apparent Strain	59
Table 4.2.1	Typical axial displacement results and standard deviations using the optical strain gauge and template matching procedure for core samples subjected to 5.78 Mpa stress	67
Table 4.3.1	Axial Strain Measurement of Aluminum	71
Table 4.3.2	Axial Strain Measurement of Granite	73
Table 4.3.3	Axial Strain Measurement of Limestone	74
Table 4.3.4	Axial Strain Measurement of Potash	75
Table 4.4.1	Aluminum Strain Measurement at 45° to the applied load.....	78
Table 4.4.2	Granite Strain Measurement at 45° to the applied load.....	79
Table 4.4.3	Limestone Strain Measurement at 45° to the applied load.....	80

Table 4.4.4	Potash Strain Measurement at 45° to the applied load.....	81
Table 4.4.5	Aluminum Strains Normal to the applied Load	83
Table 4.4.6	Granite Strains Normal to the applied Load	84
Table 4.4.7	Limestone Strains Normal to the applied Load	85
Table 4.4.8	Potash Strains Normal to the applied Load	86

LIST OF FIGURES

Figure 3.1	Displacement of surficial features on a granite test core in response to an axial pressure of 17 MPa	16
Figure 3.2	Template Matching	18
Figure 3.3	Schematic of a single-camera and a two-camera digital-optical strain gauge concept	22
Figure 3.4	Overall View of the Experimental Optical Strain Gauge	24
Figure 3.5	View of the Optical System	25
Figure 3.6	Schematic representation of X-axis rotation	33
Figure 3.7	Effect of X-axis rotation on gauge length	34
Figure 3.8	Schematic view of the experimental set-up for the X-axis micrometer calibration.....	36
Figure 3.9	Optical Lighting Arrangement.....	50
Figure 3.10	Effect of Power Supply on Image Movement.....	58
Figure 3.11	Effect of Power Supply on Apparent Strain	59
Figure 4.1a-d	Typical Optical Strain Gauge Images of Various Materials	68
Figure 4.2	Axial strain measurement of aluminum	71
Figure 4.3a	Axial strain measurement of granite.....	73
Figure 4.3b	Axial strain measurement of limestone	74
Figure 4.3c	Axial strain measurement of potash	75
Figure 4.4a	Aluminum: strain measurement at 45 ⁰ to the applied load	78
Figure 4.4b	Granite: strain measurement at 45 ⁰ to the applied load	79
Figure 4.4c	Limestone: strain measurement at 45 ⁰ to the applied load	80
Figure 4.4d	Potash: strain measurement at 45 ⁰ to the applied load	81

Figure 4.4e	Aluminum: strain normal to the applied load	83
Figure 4.4f	Granite: strain normal to the applied load	84
Figure 4.4g	Limestone: strain normal to the applied load	85
Figure 4.4h	Potash: strain normal to the applied load	86

LIST OF SYMBOLS

camera #1 reference image	I1
camera #2 reference image	I2
camera #1 post strain image	I1'
camera #2 post strain image	I2'
I1 pixel X-axis coordinate	X1 (pixel)
I2 pixel X-axis coordinate	X2 (pixel)
I1 pixel Y-axis coordinate	Y1 (pixel)
I2 pixel Y-axis coordinate	Y2 (pixel)
I1' pixel X-axis coordinate	X1' (pixel)
I2' pixel X-axis coordinate	X2' (pixel)
I1' pixel Y-axis coordinate	Y1' (pixel)
I2' pixel Y-axis coordinate	Y2' (pixel)
I1 X-axis pixel displacement (X1-X1')	$\delta X1$ (pixel)
I2 X-axis pixel displacement (X2-X2')	$\delta X2$ (pixel)
I1 Y-axis pixel displacement (Y1-Y1')	$\delta Y1$ (pixel)
I2 Y-axis pixel displacement (Y2-Y2')	$\delta Y2$ (pixel)
I1 X-axis pixel dimension	P_{X1} (μm)
I1 Y-axis pixel dimension	P_{Y1} (μm)
I2 X-axis pixel dimension	P_{X2} (μm)
I2 Y-axis pixel dimension	P_{Y2} (μm)
I1 X-axis displacement distance ($\delta X1 * P_{X1}$)	D_{X1} (μm)
I2 X-axis displacement distance ($\delta X2 * P_{X2}$)	D_{X2} (μm)
I1 Y-axis displacement distance ($\delta Y1 * P_{Y1}$)	D_{Y1} (μm)
I2 Y-axis displacement distance ($\delta Y2 * P_{Y2}$)	D_{Y2} (μm)
Active length of strain gauge	L (μm)
change in length of strain gauge	Δ (μm)

X-axis strain	ϵ_X (μ -strains)
Y-axis displacement due to X-axis rotation	ΔY (μm)
Angle of X-axis rotation	θ (degrees)
Radius of rotational circle ($L/2$)	R (μm)
Change of R due to X-axis rotation	ΔX (μm)
Change in gauge length due to X-axis rotation	ΔL_R (μm)
X-axis strain due to X-axis rotation	ϵ_{XR} (μ -strains)

CHAPTER 1: INTRODUCTION

This thesis describes a new concept for the measurement of strains. In particular, a photographic concept is described which has the potential to measure displacements with a resolution near or better than 0.1 microns, making it suitable for many strain measurement applications. The method obviates the need for contact of the sensor with the surface to be measured. This eliminates problems associated with contact and thus allows it also to be used in areas previously considered unsuitable.

CHAPTER 2: BACKGROUND

Although the measurement of strains is used in many engineering fields where the novel technique could potentially be applied, the following brief review is limited to areas of geomechanics and materials testing.

2.1 Applications

- **Stress Determinations**

Stress and stress change determinations are carried out mostly in underground mines, dams and dam foundations, underground civil engineering structures, road and railway tunnels, bridge and building foundations. The method most commonly used for in situ stress measurements is borehole overcoring (Jaegger and Cook 1979). There are various methods, all of which rely on the measurement of strains due to relaxation when a cylindrical piece of material is removed from a stressed formation such as a rock mass, a dam or a foundation.

With these methods the stresses are relieved completely at the measurement locations. The resulting strains are usually measured by the use of electrical strain gauges attached or implanted by various means on or inside the cylinder.

Another method is borehole slotting (Foruria 1987, Kanduth and Hudyma 1995) which relies on the measurement of strains at the wall of a borehole in response to the partial relaxation of the wall when a slot is cut into it. The strains are measured with a tangential strain sensor equipped with electrical strain gauges, which is pressed against the borehole wall adjacent to the slot.

- **Materials Testing**

Electrical strain gauges are often used in the field of materials testing. Usually, the mechanical characteristics, such as creep, elastic properties, expansion coefficients, etc. of materials are determined by attaching strain gauges to the surface of the test specimen, and measuring strains as the materials are subjected to various mechanical and thermal influences.

2.2 Review of Strain Measurement Techniques

2.2.1 Electrical resistance strain gauges

The majority of strain measurements techniques rely on electrical strain gauges. They work on the principle of the change of resistance of an electrical wire as a function of minute changes in its length, which is measured and used to infer the strains. In general, these devices are sturdy, precise, reliable and cheap to use. However, the technique has

several disadvantages which are listed below.

- The most important of these is that the strain gauge must be in some form of contact with the surface to be measured. This is usually accomplished by pressing against, or gluing or welding the gauge on the measuring surface. This gives rise to several problems:

-When glue is used, there is often de-bonding of the gauge in hostile environments, or when proper precautions have not been taken in its installation, or when there are large deformations. In addition, the hysteresis of the glue layer between the surface and the gauge may falsify the strain measurement.

-When the gauge is pressed against the surface (i.e., friction gauge), the problems is that when the pressure is too weak, it allows slippage and non-conformity of the gauge with respect to the strains of the surface. When the pressure is augmented, it may influence the strains of the surface as well as the behavior of the gauge.

- Another problem is the gauge's sensitivity to changes in temperature, which affects the gauge's resistivity. There are several methods to compensate for these effects, but they can be very elaborate and may not be practical in many applications, especially in rock or rock like materials.

- Due to the fact that the strains are measured in the μ -ohm range, the system is very sensitive to moisture, inductive noise, poor electrical connections (connectors have to be made of gold) and other environmental interferences.
- In long-term installations or in situations where large strains are encountered, the glue is subject to creep, which will falsify the readings or render the gauge useless.

2.2.2 Electro-optical or optical strain gauges

Although there is limited use of these types of strain gauges in mining and civil engineering, there is a large body of expertise in the field of strain measurements using the electro-optical or optical strain gauges. There are many techniques and types of strain gauges - too many to list - used in a variety of applications.

However, one thing they have in common is the use of some type of coherent light and various effects of interference in response to strains. Another common feature is the necessity for the gauge to be in contact with the surface to be measured, similar to that of the electrical strain gauges.

Consequently, all the disadvantages and problems related to contact with the surface listed previously apply to the use of electro-optical and optical strain gauges.

2.2.3 Vibrating wire strain gauges

Vibrating wire strain gauges are used to measure displacements. They work on the principle of the measurement of the change of frequency of a mechanically or electrically plucked pretensioned wire in response to changes in the pressure acting on the housing within which, or structure on which the wire is installed (Franklin 1990). Its application is mainly in long-term monitoring of stress changes in structures and is usually not used for the determination of in situ stress.

2.2.4 Laser interferometry methods for non-contact measurement of strains

There have been methods proposed which rely on principles that obviate the need of contact with the measured surface. These methods can be classified broadly into two categories, namely speckle pattern interferometry and laser holography.

The following is a brief summary of the operating principles and characteristics of the two measurement methods.

2.2.4.1 Speckle pattern interferometry

This method works on the principle that when any type of coherent radiation is reflected from, or is transmitted by a diffusing surface or medium, the resulting image takes on a speckled appearance (Lothian 1981, Gregory 1979, Chiang et al 1980, Preater 1980, Jones 1976, Vachon 1986, 1991, Leendertz 1997). This speckle pattern is caused by mutual interference of the coherent radiation because of the optical roughness of the surface or medium, and has a real existence which can be photographed or recorded.

When two such photographs or recordings are made of a surface or medium before and after some displacement has taken place, the speckle pattern of the second image is different to that of the first. When the two images are superimposed and the speckle pattern of the first image is subtracted from that of the second (either optically or electronically) the result is a series of fringes from which the amount and direction of strains can be calculated.

Speckle pattern interferometry has the capability to meet the required precision for the measurement of micro strains and would - in principle - be very suitable for in situ stress measurements and materials testing. However, the method requires the maintenance of the precise location of the optical device between the recording of the two images which makes it unsuitable for the proposed applications.

2.2.4.2 Laser holography

As the name implies, this technique produces a hologram of the surface to undergo displacement or strain by projecting a laser beam directly, and a reference beam indirectly, onto the surface with the result that a holographic image of the surface is created (Bass et al 1986, Duk-Won Park 1986, Jacoby and Williamson 1976, Ramsey 1974, Sica and Hwaling 1981, Smither et al 1988,). After strains are induced, a second hologram is made of the surface.

The two holograms are then superimposed, where the subtraction of the reference image from that of the secondary image (similar to the speckle pattern method) creates fringes which are representative of the strains the surface has undergone.

As above, the method would have the required characteristics for the proposed applications in terms of precision, but it has the same disadvantage as that of the speckle pattern interferometry method, namely that it necessitates the precise positioning of the device for the two images.

In the field of in situ stress measurements in rock, for example, where relaxation strains are induced by some mechanical work such as overcoring or cutting of a slot, it would be very difficult to maintain the exact position of the measuring device during this operation. Therefore, the method would not be feasible.

2.2.5 Optical digital image analysis techniques

2.2.5.1 Measurement of tensile strains in Brazilian test

The method most closely related to the present work uses an optical image analysis technique. Das et al (1995) reports on the application of such a method to measure strains in Brazilian tensile strength tests of lightly cemented sand specimens .

One of the methods known to determine the tensile strength of engineering materials is the Brazilian test, where a cylindrical specimen of the tested material is placed horizontally in a press and is subjected to compressive load until the specimen fails in tension diametrically in the direction of the applied load. However, in the reported work, it was also of interest to determine the diametral strains of the test specimen as the load was applied. To make this measurement, the authors employed an optical image analysis method.

Before placing the specimen under the press, a grid of reference points of approximately 0.9 mm diameter each was applied by means of spray paint onto one of the ends of the test specimen. An optical long-distance microscope was placed at a distance of 300 mm from the end of the specimen containing the reference points to obtain a magnified view of an area of 11.16 X 10.43 mm of the surface at the centre of the specimen end. Adjustments were made to the microscope to ensure its position normal to the end surface as well as to bring the surface into focus. The microscope is attached to a charge couple device (CCD)

with 480 X 512 pixels, capturing the 11.16 X 10.43 mm surface image. The digital image is sent via a frame grabber to a computer. The digital signals are then translated into an image file for analysis via commercial interactive image analysis software.

Before making any measurements, a calibration is made to obtain the scale factor relating the displacements measured on the digitized image on the computer screen to that on the actual test specimen. For any given image, corresponding to a given load, the tensile strain along the diameter of the specimen at right angles to the load is obtained by measuring the distance between two grid points located at equal distance from the centre of the end surface of the specimen and approximately 9 mm apart from one another, representing a strain gauge length of 9 mm.

The measurement is done on the computer screen using the interactive image analysis software.

Most commercial image analysis softwares are capable of resolving a pixel into eight components along each axis. Therefore, a grid line containing 512 pixels can be resolved into $(512 \times 8) = 4096$ data points. When this is used to measure the length of the test image which is 11.16 mm (11,160 μm), the maximum attainable resolution is $(11,160/4096) = 2.72$ microns per pixel along the length of the image. When expressed as strains Δ/L , that is the difference in length measured / total length of the strain gauge of 9mm, the overall resolution is

$$2^{(1)}((2.72 / 9 \times 10^3) \times 10^6) = 605.5 \mu\text{-strains} \quad (1)$$

⁽¹⁾ *2.72 μm is the resolution at each end of the strain gauge. Therefore the value has to be doubled to account for both ends of the gauge.*

Although this resolution appears to be adequate for the particular tests carried out by Das, it falls far short of the resolution required for most applications in the field of civil and mining engineering. For example, in the determination of elastic properties of rocks the required accuracy is $<5 \mu\text{-strains}$ for readings below and $<2\%$ of the reading for readings above $250 \mu\text{-strains}$ (ASTM). The resolution of the strain measurement as reported by Das could be improved by, for example, using a photonic sensor with a 30 times higher number of pixels, but at the present time such a sensor does not exist. Also, even if such a device would be technically feasible, under the current state of the art it would be very large and would be unusable in many of the proposed applications.

2.2.5.2 Video extensometer

Dorndorfer, Messphysik Laborgraete Ges.m.b.H., Austria, describes another apparatus using a digital image processing method. The apparatus is marketed as Video Extensometer ME-46.

The principle of operation is the acquisition of images of the test surface by a single 795 X 596 pixel CCD camera with a linear resolution of 4 grey scale values per pixel, before

and after the induction of strains. The test surface is marked by felt tip or marker tape to facilitate the determination and recognition of two marker points representing the length of the gauge, which can be anywhere from 50 mm to 200 mm as claimed by the manufacturer. The images are transferred to a computer via a frame grabber, where suitable software is used to determine the location of the marks before and after the induction of strains. The respective gauge lengths are computed and the strains are calculated by dividing the difference in gauge length (Δ) by the total length of the gauge (L). The linear resolution of the system is:

$$795 \text{ pixels} \times 4 \text{ (grey scale values/pixel)} = 3180 \text{ data points / line} \quad (2)$$

Based on the author's publication the shortest gauge length in his application is 50 mm where 3180 data points will result in $15.7 \mu\text{m}$ / data point. Therefore, this strain gauge length will lead to a resolution of

$$[(15.7 \times 2^{(1)}) \times 10^{-6}] / (50 \times 10^{-3}) = 628 \mu\text{-strains} \quad (3)$$

As in the case above, this is far short of the required resolution for strain measurements in materials testing or in the determination of stresses.

⁽¹⁾ *15.7 μm is the resolution at each end of the strain gauge. Therefore the value has to be doubled to account for both ends of the gauge.*

CHAPTER 3: NOVEL OPTICAL STRAIN SENSOR

In view of the difficulties and limitations associated with the methods described above, a novel method was developed and is described herein.

The method has the potential to meet the performance and the requirements of conventional strain measurement methods. Potentially it is capable of measuring strains with the required precision but with the difference that it does not have to rely on contact of the sensor with the surface to be measured. Moreover, a translation of the sensor or the test specimen will not influence the measurement of the displacements or strains. A sensor using this methodology has the capability of being operated in almost any environment and in almost any application. A description of the novel concept is given in the following section.

3.1. Operating Principle

In brief, the operating principle of the strain sensor is the digital analysis of two or more micrograph images created by charge couple device (CCD) camera(s) of the test surface. The images are apart from one another by a known distance, typically that of the length of a conventional electrical strain gauge. The digital analysis consists of measuring the relative displacements of surface features in the images as the object is subjected to

influences that cause the surface to deform. The sum of the measured displacements of features in two images divided by the distance between the two images is the strain.

What makes the method different from the digital image methods described earlier is the fact that instead of having one single image representing the entire measuring surface, two or more highly magnified images of two or more very small areas of the measuring surface are created. These are separated from one another by a known distance (in the case of the present work there are two images separated by 16 939.3 μm). The distance between the respective images constitutes the active length of the strain gauge.

In the case of the single image methods described in the previous chapter, the resolution of the strain gauge is a function of the size of the surface area which is recorded by the CCD camera, and the number of pixels/line contained in the photonic receptor of the CCD camera. As was demonstrated in the previous two examples, this method gave maximum resolutions of 2.72 μm per pixel or 604 μ -strains for a 9 mm strain gauge, and 15.73 μm per pixel or 628.9 μ -strains for a 50 mm strain gauge respectively. In contrast, in the novel concept described herein, and in the subsequent experimental apparatus used to validate the method, the two images have a high number of pixels representing a small surface area. With an image length of 0.4 mm (400 μm), a photonic sensor having 640 pixels/line, a pixel resolution of 8 and a strain gauge length of 16 939.3 μm , as is the case in the experimental apparatus, the resolution is

$$400/(640 \times 8) = 0.078 \text{ } \mu\text{m/pixel} \quad (4)$$

or

$$2(0.078) \times 10^6 / 16\,939.3 = 9.2 \text{ } \mu\text{-strains} \quad (5)$$

It can be seen that the pixel resolution is significantly higher and is not influenced by the length of the strain gauge. In fact, contrary to the single image method, where the pixel resolution is proportional to the size of the image and the strain resolution remains constant, in the multi image method the pixel resolution is constant but the strain resolution is inverse proportional to the length of the gauge.

Technically, the method takes advantage of the fact that when an object is subjected to influences that causes it to deform, the strain will result in a corresponding displacement of surface features. For example, when compressive load is applied axially onto a core specimen, the core will become shorter in the direction of the load and will cause the axial distance between surface features on the side wall of the core to shorten. When images of two areas along the axis of the core side wall are produced before and after the application of the load, the positions of the surface features in the images will have changed relative to each other. This displacement of the surface features can be seen in the example shown in Figure 3.1 where two 0.4 x 0.3 mm large images, separated axially from one another by 16 939.3 μm , of the side wall of a granite core sample are taken before the load was applied and after the specimen was subjected to an axial charge of 17 MPa. When the subsequent change in location of the surface features is measured, it will



Granite surface image at 0 MPa



Granite surface image at 17 Mpa

Figure 3.1 Displacement of surficial features on a granite test core in response to an axial pressure of 17 MPa

be found that the total distance between the features, as measured in the reference images, will have become shorter in the secondary images (after the load is applied). The change in distance divided by the total distance by which the two images are separated from one another is the strain. The measurement of the displacements of surface features is done by a method called "template matching" which is described in the following section.

3.1.1 The principle of "Template Matching"

Basically, template matching is a computer program that is capable of determining the location of features in a digital image and finding and determining the new location of the same features in a subsequent image. The method works by placing an imaginary square of a suitable size (usually a fraction of the total image), called a template, anywhere on the area of a reference image as shown in Figure 3.2, and recording and storing the grey scale sequence of pixels contained in this square together with the pixel XY coordinate of one of the corners, usually the top left corner of the template. Video cameras are designed to sweep (read) images starting at the left pixel of the top line, and sweeping the lines left to right from the top line to the bottom line. The coordinate system follows this convention with the point of origin being the top left pixel, the X-axis coordinate being the pixel number on the horizontal line, and the Y-axis coordinate being the line number. The same sweeping and coordinate convention is used to record the pixel sequence in the template. The computer then searches for the matching grey scale sequence in a

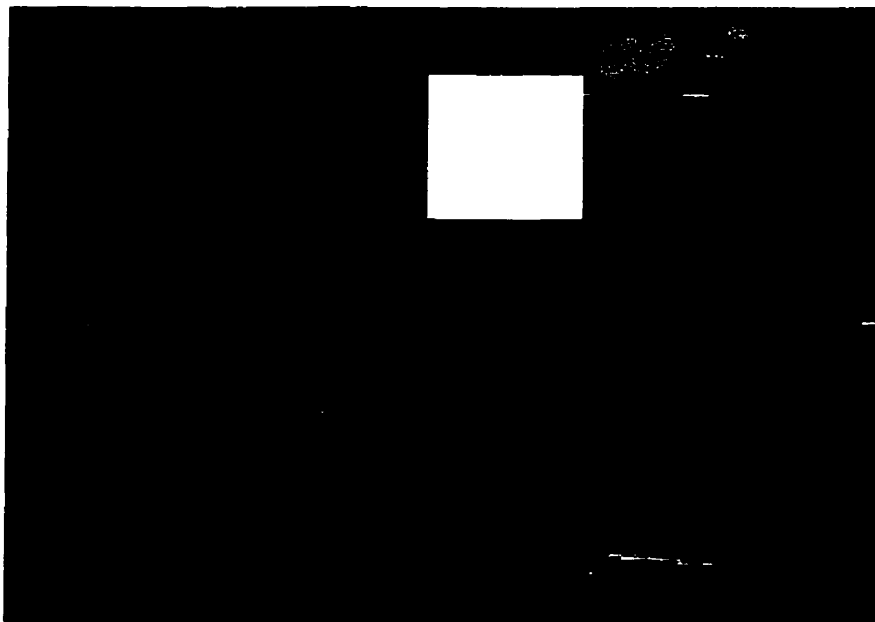


Figure 3.2 a shows a template placed on a granite surface image with the test core at 0 MPa

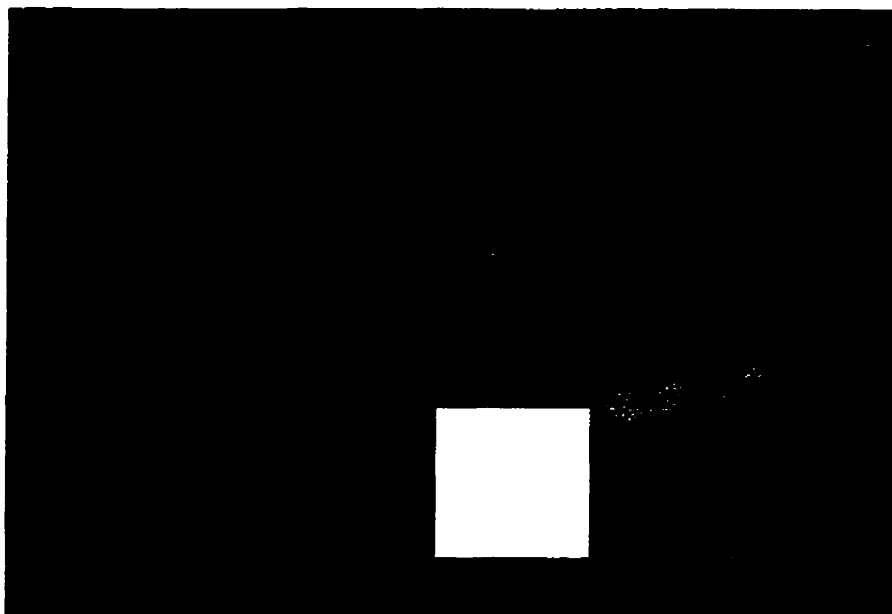


Figure 3.2 b shows the new location of the template when the test core was loaded to 17 Mpa

Figure 3.2a and 3.2b Template Matching

subsequent image and records the new X'Y' coordinate of the template. Thus, for example, if a photonic sensor has 480 lines (Y-axis) of 640 pixels each (X-axis), and the upper left corner pixel of the template is number 30 on line number 10, the coordinate would be X30, Y10. If the new location has a coordinate of X'60, Y'30, then the template has moved 30 pixels on the X-axis and 20 pixels on the Y-axis with a resultant displacement of

$$\sqrt{30^2 + 20^2} = 36 \text{ pixels} \quad (6)$$

The computer program is capable of recognizing white and 251 grey scale values. This is used to assign a value to each pixel, which in turn allows the linear pixel resolution to be enhanced by a factor of up to eight using Fourier transform algorithms. The grey scale sequence in a template is relative, and for the search and recognition of a particular template in a subsequent image, the computer compares not the absolute grey scale values but the relative ratios in the sequence, a process which is termed "normalization". This has the advantage that features can be recognized even when the subsequent image has a different grey intensity (change in illumination) or has changed in contrast (change in focus).

3.1.2 Image acquisition

There are several methods and configurations by which images can be obtained, each with its advantages and disadvantages.

In one of the possible configurations the images are obtained by means of a single, high-resolution CCD camera and a suitable optical arrangement which permits selected parts of the surface, which are separated from one another by a known fixed distance, to be photographed simultaneously. One of these configurations is shown in Figure 3.3 where a single camera acquires a split image of two areas of the object by an arrangement of two rhomboid prisms. Other prism arrangements would allow the acquisition of three or more split images. The advantage of such arrangements is that there is only one single camera acquiring the split images simultaneously, which virtually eliminates the effects of float, compression and jitter and assures the maintenance of the distance between the images. Another advantage is that it would be more amenable to packaging in a borehole instrument. Since the image is split into two or more components, one disadvantage is that the CCD camera would have to have a large pixel capacity in order to have a sufficient number of pixels available for each split image.

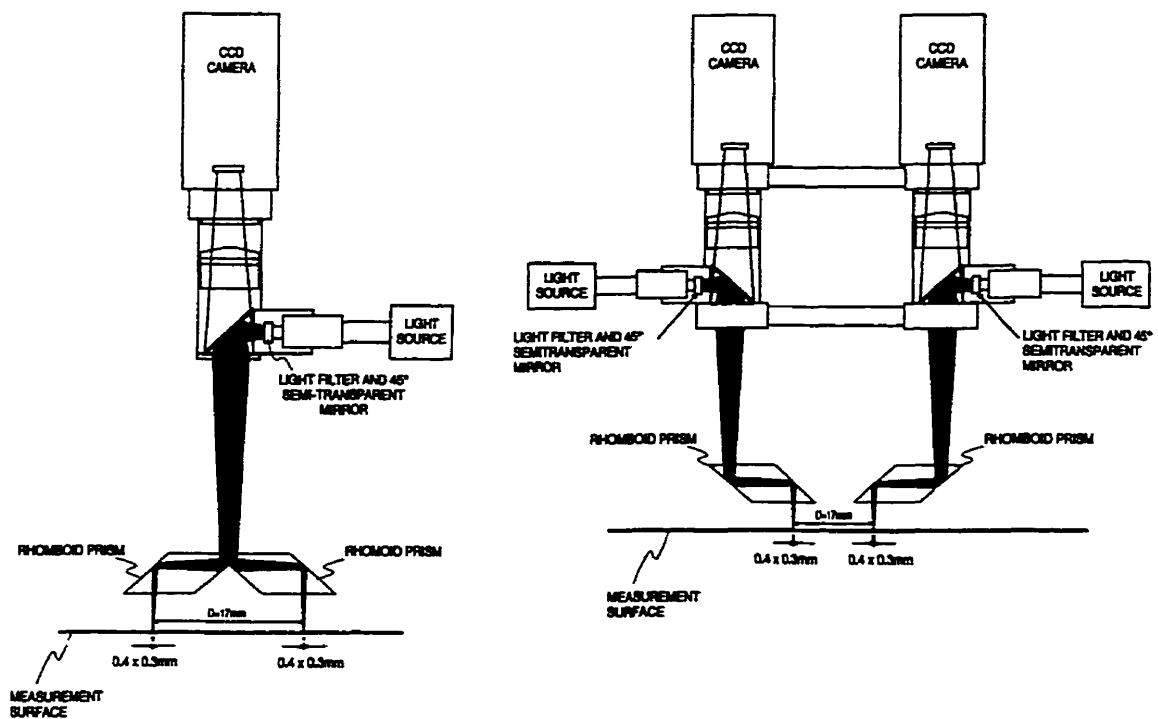
In another possible configuration, two or more CCD cameras are used in conjunction with suitable optical equipment arranged at fixed distances from one another, which permits two or more areas of the surface to be photographed. In this case, the photonic

sensor arrays of each camera acquires the image of a small surface area, and therefore the surfaces are represented by a larger number of pixels. This, in turn, results in a higher pixel resolution and hence in a higher strain gauge precision.

A two-camera configuration is shown in Figure 3.3.

However, there are disadvantages in using multi-camera systems. Since the cameras are independent from one another, the effect of float, compression and jitter is considerably higher, which can lead to higher inaccuracies. Another disadvantage is that the maintenance of the distance between the images is more difficult since the assembly is more sensitive to mechanical and thermal effects which may cause shifts in the distance between the cameras. In addition to this, the multi-camera arrangement would be difficult to package in a borehole instrument.

It is certain that there are other systems and configurations which might perform better than the ones described above. However, the optimization of the methodology and the equipment is beyond the scope of the present work and the expertise of the author.



The schematic shows a single CCD camera and a two CCD camera system with lens arrangement and prisms that allows the acquisition of a magnified split image in the former system and two independent magnified images in the latter system. Images are produced of two areas of the surface which are separated from one another by app. 17 mm. The size of the photographed surfaces is 0.4 x 0.3 mm. The surfaces are illuminated co-axially by light introduced through a 45⁰ semitransparent mirror into the optical tube.

Figure 3.3 Schematic of a single-camera and a two-camera digital optical strain gauge concept

3.2 Experimental Apparatus

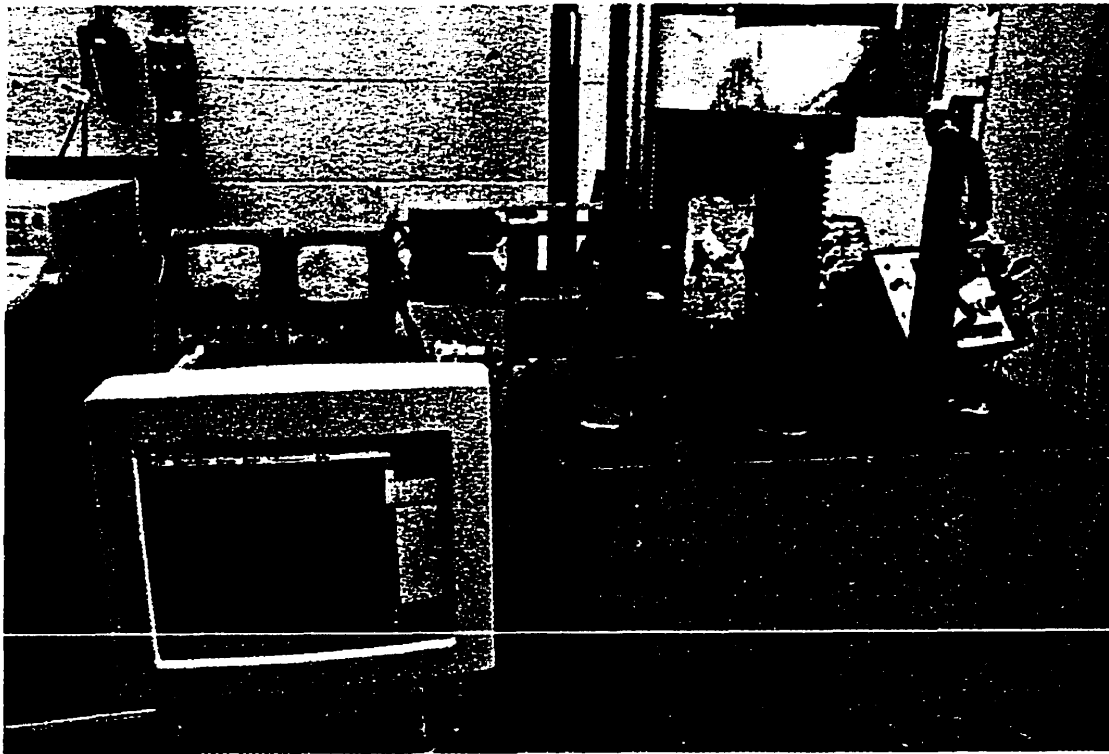
In order to confirm the viability of the concept, an experimental apparatus was constructed that would be capable of measuring strains of test specimens under load, simulating test procedures that are employed in the determination of mechanical properties of materials such as the modulus of elasticity and the Poisson's ratio.

The apparatus was intended for the validation of the principle only and not for the optimization of the technique. However, it was hoped that, in addition to this objective, the experimental work would be able to expose some of the characteristics, parameters and quirks which would help in the optimization of the method.

The experimental apparatus is shown in Figures 3.4 and 3.5 while details of the apparatus are given below.

3.2.1 Hardware

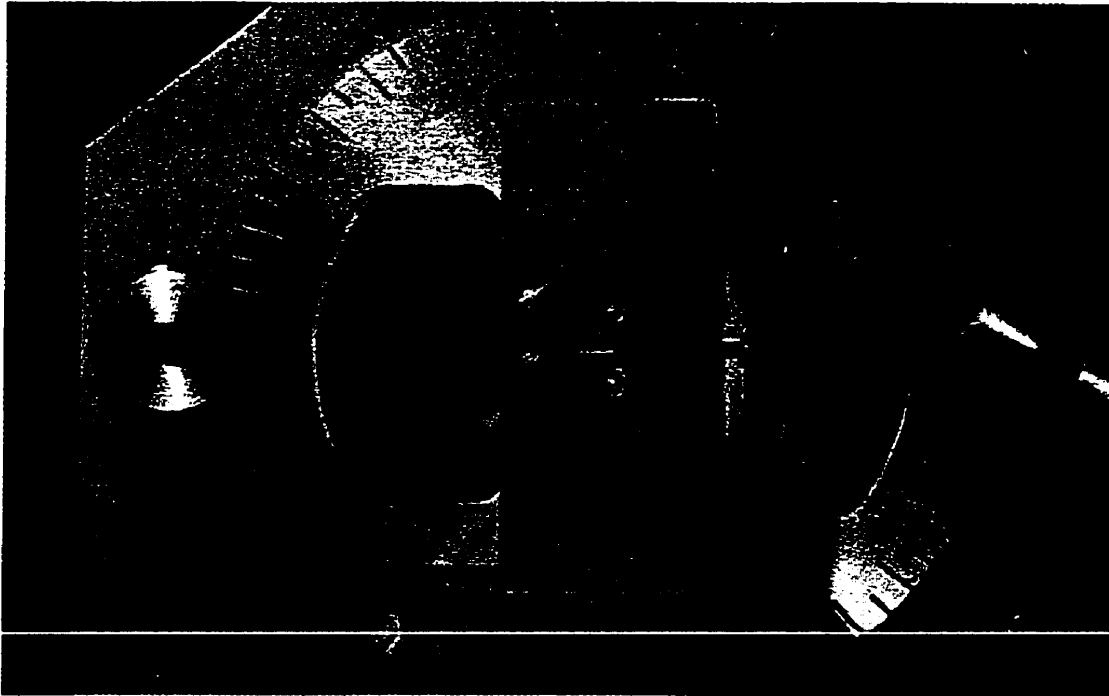
The apparatus consists of two parallel arranged black & white NUVI-SPEC CCD cameras equipped with 4.8 mm X 3.6 mm photonic detectors comprising 480 lines of 640 photonic sensors per line. The cameras are powered by two 12 VDC batteries connected in series to deliver 24 to 25 VDC.



The figure shows a strain gauge instrumented concrete core specimen under compression in a hydraulic press. The experimental optical sensor consists of a two-camera system which is seen photographing the side of the core next to one of the electrical strain gauge rosettes. The two separate images of the 0.4 x 0.3 mm surfaces can be seen on the TV monitors with one of the images displayed on the computer screen.

Figure 3.4 Overall View of the Experimental Optical Strain Gauge

Attached to each camera is an OPTICA MML12 (16 mm focal length, 12X magnification) optical magnifying tube and an EALING 24-1489 rhomboid 20 mm prism. This enables each camera to photograph an area of approximately 0.4 mm X 0.3 mm of the surface of an object at a magnification of 12. Thus, two images of the surface are created which are separated from one another by a fixed distance of approximately 17 mm.



The front view of the optical sensor shows the rhomboid prism arrangement with co-axial lighting (which was found to be insufficient for the experiments). The optical assembly is installed on the graduated rotating disk which allows it to be rotated by 360° .

Figure 3.5 View of the Optical System

The assembly is installed on a frame which keeps the cameras at a fixed distance from one another. The frame also has a provision which allows it to be rotated axially by 360° as seen in Figure 3.5. The frame is mounted on a MITUTOYO micrometer stage, which allows the complete assembly to be displaced horizontally by 1 inch in the X- and Y-axis with a 0.0001 inch resolution. The image focus is adjusted with the Y-axis micrometer while observing the images on closed-circuit TV monitors. The X-axis micrometer is used to move the assembly horizontally and parallel with the test surface in order to scan the object surface in search for areas that have good contrast features.

3.2.2 Image and data processing hardware and software

The images are captured and digitized with a CORECO version 2.40 frame grabber in conjunction with an ATI VRAM Mach 4 graphics accelerator card installed in a COMPAC Pentium Pro desk-top computer. The images are stored in .TIF file format.

The MATROX ITOOLS INTERACTIVE program was chosen for the search and location of the templates. Preliminary research (Coulombe 1995) has indicated that this software is the most robust and versatile of the commercial image processing softwares, providing a linear pixel resolution of $1/8$, with the potential to improve this resolution to better than $1/10$ by using Fourier Transform routines. The program has an extensive library of routines, which allowed the interactive creation of the "template matching" method.

The experimental procedure consists of the following steps:

- on the reference images of camera #1 and #2 selecting an area of 150×150 pixels each as a template, reading and storing the grey-scale sequence of the templates and determining the XY coordinates of the pixel forming the upper left corner of the templates,
- searching for the same templates on the secondary images of both cameras, determining the new X'Y' coordinates and subtracting these from the reference coordinates,

- returning to the reference images, placing another template each on a different location on the images, repeating the grey-scale and coordinate determination and the search for the templates on the secondary image,
- repeating the procedure for a total of 15 times
- reversing the procedure and searching on the reference images the templates established on the secondary images, and repeating this procedure 15 times.

The computer is programmed to automatically subtract the X'Y' coordinates from the XY coordinates for each template matching procedure and writes the coordinate difference to a text file. Since the 15 template matching procedures are repeated in the reverse order, the text file contains 2 sets of 15 coordinate difference values each for the first image X- and Y-axis, representing one end of the strain gauge, and two more sets of 15 coordinate difference values for the second image X- and Y-axis, representing the other end of the strain gauge.

3.3 Calculations

3.3.1 Glossary of nomenclature, symbols, terms and conventions

The following is a glossary of the nomenclature, symbols, terms and conventions used in the calculations to derive strains from tests with the digital optical strain sensor.

Since the experimental apparatus consists of camera #1 acquiring an image at one end of the strain gauge, and camera #2 on the other end, and that the procedure is repeated after the strain has occurred, the following convention is used to identify the images:

camera #1 reference image	I1
camera #2 reference image	I2
camera #1 post strain image	I1'
camera #2 post strain image	I2'

The following symbols are used for the identification of the coordinates in the pixel coordinate system:

I1 pixel X-axis coordinate	X1 (pixel)
I2 pixel X-axis coordinate	X2 (pixel)
I1 pixel Y-axis coordinate	Y1 (pixel)
I2 pixel Y-axis coordinate	Y2 (pixel)
I1' pixel X-axis coordinate	X1' (pixel)
I2' pixel X-axis coordinate	X2' (pixel)
I1' pixel Y-axis coordinate	Y1' (pixel)
I2' pixel Y-axis coordinate	Y2' (pixel)

The following symbols are used for the pixel displacements in pixel units:

I1 X-axis pixel displacement (X1-X1')	$\delta X1$ (pixel)
I2 X-axis pixel displacement (X2-X2')	$\delta X2$ (pixel)
I1 Y-axis pixel displacement (Y1-Y1')	$\delta Y1$ (pixel)
I2 Y-axis pixel displacement (Y2-Y2')	$\delta Y2$ (pixel)

The following symbols are used for the pixel dimensions in μm :

I1 X-axis pixel dimension	P_{X1} (μm)
I2 X-axis pixel dimension	P_{X2} (μm)
I1 Y-axis pixel dimension	P_{Y1} (μm)
I2 Y-axis pixel dimension	P_{Y2} (μm)

The following symbols are used for displacement distance in μm :

I1 X-axis displacement distance ($\delta X1 * P_{X1}$)	D_{X1} (μm)
I2 X-axis displacement distance ($\delta X2 * P_{X2}$)	D_{X2} (μm)
I1 Y-axis displacement distance ($\delta Y1 * P_{Y1}$)	D_{Y1} (μm)
I2 Y-axis displacement distance ($\delta Y2 * P_{Y2}$)	D_{Y2} (μm)

Other terms:

Active length of strain gauge	L (μm)
Change in length of strain gauge	Δ (μm)
X-axis strain	ϵ_X (μ -strains)
Y-axis displacement due to X-axis rotation	ΔY (μm)
Angle of X-axis rotation	θ (degrees)
Radius of rotational circle ($L/2$)	R (μm)
Change of R due to X-axis rotation	ΔX (μm)
Change in gauge length due to X-axis rotation	ΔL_R (μm)
X-axis strain due to X-axis rotation	ϵ_{XR} (μ -strains)

3.3.2 Strain calculations

In order to obtain the highest possible resolution, the cameras of the experimental apparatus are rotated so that the photonic sensors' X-axes (640 pixels) are aligned with the longitudinal axis of the optical strain gauge. Therefore, the photonic sensor's X-axis measures longitudinal displacements and the Y-axis measures lateral displacements relative to the axis of the optical gauge.

Normally, when the strains are calculated, the Y-axis displacements are not included in the calculation since, in most cases, these are similar in both, the #1 and the #2 image, thus cancelling each other. However, it is possible that a test specimen undergoes a rotation when the load is applied, resulting in Y-axis displacements that are different between the two images. When this is the case, its effect on the strain reading has to be evaluated by including the Y-axis displacements in the calculations.

With this in mind, the following section discusses two methods to calculate strains, namely i) X-axis strain if the Y-axis displacements are nearly similar in both images and ii) X-axis strain if the Y-axis displacements are dissimilar.

Case 1: X-axis strain (without rotation)

As mentioned above, the text file contains two sets each of 15 $\delta X1$ and 15 $\delta X2$ values. The following statistical procedure is first applied for the calculation of the pixel displacements:

- the average and the standard deviations are calculated for each set
- the sets with the lower standard deviations in each, the $\delta X1$ and $\delta X2$ series are used for the calculations
- in each of the two series the values that deviate by more than one standard deviation are excluded
- the remaining values are used to arrive at a new average for $\delta X1$ and $\delta X2$

To calculate X-axis strains, the following equations are used:

$$D_{X1} = \delta X1 * P_{X1} \quad (7)$$

$$D_{X2} = \delta X2 * P_{X2} \quad (8)$$

$$\Delta_X = D_{X1} - D_{X2} \quad (9)$$

$$\epsilon_X = \Delta_X / L \quad (10)$$

These equations can be combined to give the following equation:

$$\epsilon_X = \frac{(\delta X1 * P_{X1}) - (\delta X2 * P_{X2})}{L} \quad (11)$$

Case 2: X-axis strains (with rotation)

The calculations for the effect on the strain gauge length (L) of a rotation of the test specimen, or the rotational misalignment of the optical strain gauge with respect to the direction of the applied load, are valid only for cases where the fulcrum of the rotation is assumed to be at the axial center of the test specimen.

First δY_1 and δY_2 are derived by the same statistical procedure used to calculate the X-axis displacement. To arrive at the Y-axis displacement distances, the following equations are used:

$$D_{Y1} = \delta Y_1 * P_{Y1} \quad (12)$$

$$D_{Y2} = \delta Y_2 * P_{Y2} \quad (13)$$

The following equation solves for the Y-axis displacements due to X-axis rotation:

$$\Delta Y = D_{Y1} - [(D_{Y1} + D_{Y2})/2] \quad (14)$$

To arrive at the corrected strain gauge length the following equations are used (refer to Figure 3.6):

First, the angle of rotation θ is derived by

$$\theta = \arcsin (\Delta Y / R) \quad (15)$$

where R is L/2. The difference in length of R expressed as ΔX is derived by

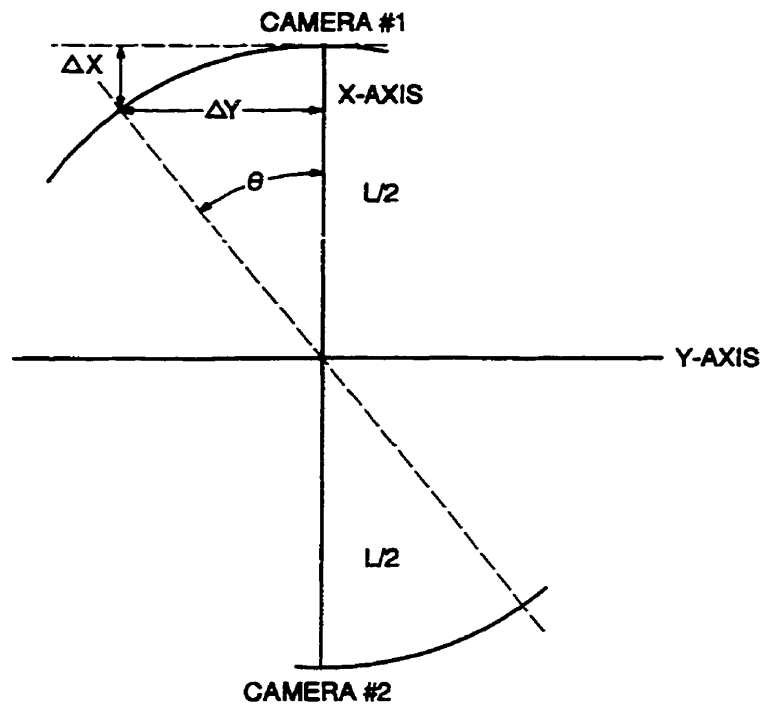
$$\Delta X = R(1 - \cos \theta) \quad (16)$$

and the difference in the length L of the strain gauge (ΔL_R) is

$$\Delta L_R = 2\Delta X \quad (17)$$

which, expressed in μ -strains (ϵ_{XR}), is

$$\epsilon_{XR} = (\Delta L_R * 10^6) / L \quad (18)$$



The figure shows the normal positions of the cameras and the effect on the length of the X-axis when the cameras are rotated. ΔY denotes the Y-axis displacement as a function of X-axis rotation, and ΔX is the distance by which the X-axis is shortened as a function of this displacement.

Figure 3.6 Schematic representation of x-axis rotation

3.3.3 Effect of rotation on strain gauge length

The effect of different angles of X-axis rotation on the length of the strain gauge is shown in Figure 3.7. The results show that the effect of the rotation of the X-axis either through rotation of the test specimen during initial loading, or by misalignment of the gauge's X-axis with respect to the direction of the applied load, is significant. At a rotational angle of 0.3° the length of the strain gauge is already decreased by $13.7 \mu\text{-strains}$ (greater than the nominal resolution of the strain gauge), while for example a rotation of 1° and 5° will result in the decrease of the gauge length by 152 and $3805 \mu\text{-strains}$ respectively. In view of this it is imperative that the Y-axis deviations be closely monitored during the test work.

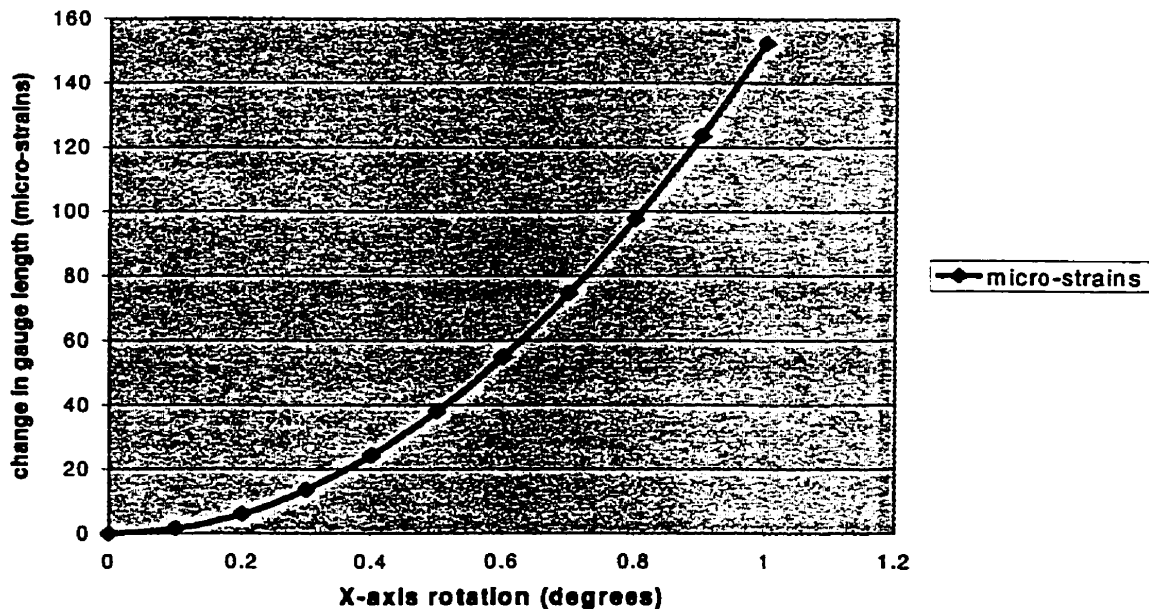


Figure 3.7 Effect of x-axis rotation on apparent change of gauge length

3.4 Characterization of Experimental Apparatus

Before work could be started for the validation of the strain measurement method, work was carried out for the characterization of the apparatus. In particular, it was essential that the image size, the pixel dimensions and the distance between the two images be determined. In addition, the effects of lighting, the contrast of features in the images etc. on the performance of the template matching procedure had to be established. Parameters such as the effect of the type of power supply on image stability were also determined. The following sections give details on the work to characterize the experimental apparatus.

3.4.1 Micrometer calibration

The optical strain gauge is mounted on a micrometer stage which can be slid horizontally in the X and Y axes by means of a high-precision micrometer screw set having a nominal resolution of 0.0001 inches (2.54 μm) / division. Since the X-axis micrometer was to be used as a calibration for the determination of the image sizes, the distance between images and the pixel dimensions, its precision needed to be verified. A test was therefore carried out to determine the precision of the X-axis micrometer screw. The details of the test and the results are given below.

3.4.1.1 Experimental set-up

In order to carry out the verification of the precision of the micrometer screw, a feeler gauge (Mitutoyo) with a precision of 0.0001 inches (2.54 μm) / division and a range of 0.008 inches was used, against which the micrometer screw was calibrated. The experimental set-up is shown schematically in Figure 3.8. The feeler gauge was positioned in such a way that it could measure the horizontal movement of the micrometer stage in the X-axis as the transverse micrometer was turned.

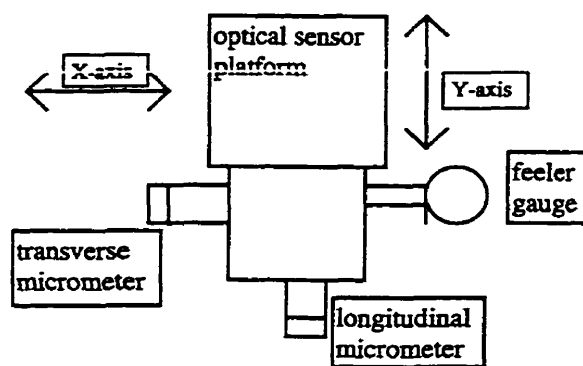


Figure 3.8 Schematic view of the experimental set-up for the X-axis micrometer calibration

3.4.1.2 Test

The feeler gauge was adjusted to zero at a micrometer reading of 0.7000 inches, and the micrometer was then turned in increments of 0.0010 inches, displacing the micrometer stage in the X-axis by a corresponding distance. The reading of the feeler gauge was

taken at each increment and was compared to the X-axis translation as imparted by the micrometer. Table 3.4.1 shows the results.

The results show that the micrometer displacement as indicated by the screw graduation is analogous to the actual displacement as indicated by the feeler gauge. Therefore, the displacement of the micrometer stage can be measured at a precision of 2.54 μm , and it is well suited as a means for calibrating the measurement of displacement as determined by the optical sensor.

Table 3.4.1 X-Axis Micrometer Calibration

micrometer reading (in)	δD (in)	feeler gauge reading (in)	Δ Reading
0.7000	0	0.0000	0
0.7010	0.0010	0.00095	0.00005
0.7020	0.0020	0.0020	0
0.7030	0.0030	0.0030	0
0.7040	0.0040	0.0040	0
0.7050	0.0050	0.0050	0
0.7060	0.0060	0.0060	0
0.7070	0.0070	0.0070	0
0.7080	0.0080	0.0080	0

3.4.2 Determination of linear pixel dimensions

The pixel dimensions for the experimental apparatus, as derived by the following equations, are nominally 0.625 μm in the X-axis and the Y-axis respectively for both cameras:

$$P_X = 400/640 \quad (19)$$

$$P_Y = 300/480 \quad (20)$$

Where P_X and P_Y are the pixel dimensions in the X-axis and the Y-axis respectively, the X-axis and Y-axis image sizes are 400 μm and 300 μm respectively, and the photonic sensor X-axis and Y-axis number of pixels are 640 and 480 respectively. However, the configuration of the optical sensor and the high precision essential for strain measurements requires that the linear pixel dimensions are determined experimentally. For this purpose, a test series was conducted to compare the X-axis and Y-axis displacements as measured with the apparatus against displacements measured with the calibrated micrometer described in Section 3.4.1.

3.4.2.1 Test procedure

The experiment was carried out using the side of a granite diamond drill core specimen having a diameter of 100 mm. The specimen was placed upright and centrally before the

experimental apparatus, and the apparatus' X-axis micrometer stage was moved horizontally in increments of 25.4 μm . This had the effect that the images of the surface of the test specimen, as seen by the cameras, was displaced horizontally by an equal distance. At each increment, the surface images of both fields of vision were digitally recorded. For the Y-axis calibration, the apparatus was in a vertical position with the camera objectives aligned vertically relative to each other, while for the X-axis calibration, the apparatus was rotated by 90° with the camera objectives aligned horizontally relative to each other.

The displacements recorded by the photographic method were determined by template matching and were then compared with the actual incremental displacements of the micrometer stage as applied by the calibrated micrometer screw. To arrive at the average displacement values, the statistical method described in Section 3.3.3.2 was used.

3.4.2.2 Test results

The test results for the X-axis and Y-axis calibration are shown in Table 3.4.2.1 and Table 3.4.2.2 respectively. The tables show the template matching data for the images created by each of the two cameras. The first column is the cumulative lateral displacement of 25.4 μm increments applied to the apparatus by the micrometer screw, the second column shows the cumulative displacement measured for image #1 by the

apparatus with column three showing the increments. The fourth and fifth column shows the respective measured displacements for image #2.

Table 3.4.2.1 X-Axis Pixel Dimension Measurement

cumulative displacement applied	image #1		image #2	
	cumulative displacement measured	incremental displacement measured	cumulative displacement measured	incremental displacement measured
μm	μm	μm	μm	μm
25.4	23.8	23.8	24.8	24.8
50.8	48.0	24.2	50.0	25.1
76.2	72.4	24.4	75.9	26.0
101.6	96.7	24.3	101.7	25.8
127	120.5	23.8	126.5	24.9
152.4	145.2	24.7	152.1	25.6
177.8	169.6	24.4	177.5	25.4
203.2	193.8	24.3	203.1	25.6
228.6	219.1	25.3	228.9	25.8
254	243.0	23.9	253.8	24.9
Average		24.3		25.4

The tables show that there are variations within the measured increments. This is attributed to the fact that it was difficult to accurately align the micrometer scale marks with the hatch mark. In view of this it was decided to use the cumulative measured displacements for calculating the pixel dimensions.

In the case of the X-axis calibration, the results show that the cumulative displacement measured by the optical sensor is 95.663% for image #1 and 99.918% for image #2 of that applied to the apparatus by the micrometer screw. In the Y-axis calibration test, image #1 and image #2 yielded sensor measurements which were 95.716 % and 95.962 % respectively lower than the applied displacement.

Table 3.4.2.2 Y-Axis Pixel Dimension Measurement

cumulative displacement applied	image #1		image #2	
	cumulative displacement measured	incremental displacement measured	cumulative displacement measured	incremental displacement measured
μm	μm	μm	μm	μm
12.7	11.7	11.7	11.7	11.7
25.4	23.9	12.2	24.4	12.7
38.1	36.9	13.0	37.4	13.0
50.8	48.7	11.8	49.1	11.7
63.5	61.0	12.3	61.4	12.3
76.2	72.5	11.4	72.8	11.4
88.9	84.9	12.4	85.5	12.7
101.6	97.2	12.3	97.9	12.5
114.3	110.8	13.6	111.5	13.6
127	121.2	10.3	121.9	10.4
139.7	133.7	12.5	134.1	12.1
Average		12.2		12.2

3.4.2.3 Conclusion

The objective of the test series was to determine the actual linear dimension of the pixels both in the X-axis and the Y-axis. The accurate determination of these values, particularly in the X-axis which is the principal axis of strain measurements, is essential for the determination of strains in materials testing and the determination of stresses and stress changes in the field of mining and civil engineering. The linear dimension P_X and P_Y for the experimental apparatus is nominally $0.625 \mu\text{m}$ (see above). The tests have determined the correction factor to be applied for both axes. The following calculations are used to arrive at the corrected values for P_X and P_Y :

$$P_{X1} = 0.625 / 0.95663 = 0.65334 \mu\text{m} \quad (22)$$

$$P_{X2} = 0.625 / 0.99918 = 0.62551 \mu\text{m} \quad (23)$$

$$P_{Y1} = 0.625 / 0.95716 = 0.65297 \mu\text{m} \quad (24)$$

$$P_{Y1} = 0.625 / 0.95961 = 0.65131 \mu\text{m} \quad (25)$$

3.4.3 Determination of the optical strain gauge length

The object of the test series was to determine the precise distance L between $I1$ and $I2$ in order to be able to calculate ϵ using equations 10 and 11. To carry out the determination, the apparatus was positioned so that the camera objectives were aligned horizontally relative to each other. The apparatus' micrometer stage was moved horizontally using the calibrated micrometer screw of the stage's X -axis. The vertical edge of a machined metal block was used as the optical target, and the apparatus was moved laterally relative to the edge. Micrometer readings were taken with the target edge visible at one extreme, the center and the other extreme of the first image and then at the same positions in the second image. The experimental data are and the results are shown in Tables 3.4.3.1 and 3.4.3.2 respectively.

Table 3.4.3.1 Measurement of Distance between the Two Images of the Experimental Optical Strain Gauge

Edge Position	Micrometer Reading
left image, left edge	0.9350 inch
left image, center	0.9273 inch
left image, right edge	0.9195 inch
right image, left edge	0.2681 inch
right image, center	0.2604 inch
right image, right edge	0.2526 inch

Table 3.4.3.2 Test Results for the Determination of the Gauge Length

Target Edge Position in the Images	Gauge Length (L)	
	inches	millimeter
left edge to left edge	0.6669	16.9393
center to center	0.6669	16.9393
right edge to right edge	0.6669	16.9393

3.4.4 Summary of characteristics of the experimental optical strain gauge

With the results of the calibrations in the previous sections it is now possible to arrive at the characteristics of the optical strain gauge. These are given in Table 3.4.4

Table 3.4.4 Summary of Characteristics of the Experimental Optical Strain Gauge

P_{X1}	0.65334 μm
P_{X2}	0.62551 μm
P_{Y1}	0.65297 μm
P_{Y2}	0.65131 μm
X-axis Pixels /Line	640
Y-axis Number of Lines	480
Linear Pixel Resolution	8
X-axis Data Points	(640 x 8) 5120
Y-axis Data Points	(480 x 8) 3840
I1 Dimension	(0.65334 x 640) 418 μm x (0.65297 x 480) 313 μm
I2 Dimension	(0.62551 x 640) 400 μm x (0.65131 x 480) 312 μm
I1 X-axis Resolution	(418/5120) 0.0816 μm
I1 Y-axis Resolution	(313/3840) 0.0815 μm
I2 X-axis Resolution	(400/5120) 0.0781 μm
I2 Y-axis Resolution	(312/3840) 0.0814 μm
Length of Optical Gauge (L)	16939.3 μm
Strain Gauge Resolution (X-axis)	(0.0816 + 0.0781)* 10^6 /16939.3 = 9.43 μ -strains

3.5 Effect of the Angle of Incidence of Lighting

3.5.1 Introduction

The images created by the optical strain gauge reproduce areas of the test surfaces of approximately 0.4 mm x 0.3 mm each. The images are then magnified by a factor of 12 before they are stored digitally and subsequently analyzed. The surfaces subject to analyses are not smooth and highly polished as, say, that of a microscope specimen, but have a rather coarse texture. Because of the magnification, a typical machined metal specimen, for example, will display large cutting grooves, a diamond drill rock core sample or the side wall of a borehole will appear to have large asperities (see Figures 4.1a-4.1d).

In view of this fact, it stands to reason that the angle of incidence of lighting on the object surfaces will have an effect on the apparent location of surficial features on the image. In fact, some features may appear to be displaced by several microns when changing the angle of incidence of lighting from, for example, 45° to 20° relative to the surface.

In order to determine the effect of angle of incidence of lighting on the apparent displacement of surficial features in the images, and how this is affected by different materials, a series of tests was conducted, which is described below.

3.5.2 Determination of the effect of changes in the angle of incidence of lighting

The test apparatus consists of the optical strain gauge. The light is provided by a Fostec DCR II regulated light source with an EKE quartz halogen lamp with the energy peak at a wavelength of approximately 700 nm and virtually zero energy at 750 nm when equipped with an interface infrared filter. As a consequence, the light is quasi monochromatic, which enhances the resolution of the image. The filter has the additional effect of filtering out radiation in the infrared region where white light has its highest thermal energy, thus delivering "cold" light.

The light is transmitted via a 20-inch fiber optic cable into a Fostec A08900 fiber optic light line. The fiber optic light transmission eliminates any radiant heat from the light source and thus, the only thermal effect originates from the light color temperature, which is negligible with the infrared filter in place. Attached to the light line is a 5-inch cylindrical lens (Fostec A08836) for light intensity increase.

For the purpose of the tests, two angles of incidence of light were used which, due to space constraints and practical feasibility, were chosen at 45° and 20° relative to the surface of the test specimen. The light was placed in such a way that it illuminated the specimen surface with a well defined 120 mm long vertical light bar with a width of approximately 8 mm for the 45° and 15 mm for the 20° angle respectively.

The test specimens were cylindrical rods in the case of metals and HQ diamond drill cores in the case of other materials such as rocks and concrete. The dimensions of the specimens were approximately 100 mm diameter with a length to diameter ratio of 2:1. For the tests, the specimens were centered in an upright position in front of the apparatus, with the camera objectives positioned normal to the surface in a vertical configuration.

The following materials were used:

granite
limestone
potash
concrete
aluminum
stainless steel

The test procedure consisted of first photographing the specimen surface at a lighting angle of 45° and then at an angle of 70° relative to the plane of the surface, and computing the apparent displacement of surficial features in the upper and lower image. The computation of the apparent pixel displacement (δX and δY) was done by template matching and the statistical procedure described in Section 3.3.3.2. To arrive at the displacement distances D_{X1} and D_{X2} , equations 7 and 8 were used. The results of the test work are presented in the following section.

3.5.3 Experimental results

The apparent displacement of surficial features as a function of the angle of incidence of light relative to the specimen surface for each material is given in Table 3.5.1. The table shows that the limestone specimen is the most sensitive of the materials to change of the angle of incidence of light, followed by aluminum. In the middle of the spectrum are concrete and granite while steel and potash show only little effect to changes of angle.

Table 3.5.1 Apparent Displacement of Surficial Features as a Function of the Angle of Incidence of Light

MATERIAL	APPARENT DISPLACEMENT (μm)			
	I1 X-axis	I2 X-axis	I1 Y-axis	I2 Y-axis
ALUMINUM	-2.14	-1.44	-3.30	-2.31
CONCRETE	-0.21	-1.80	-2.26	-2.71
GRANITE	-0.06	-2.64	-0.01	-3.15
LIMESTONE	-4.61	-5.67	-9.77	-12.25
POTASH	0.10	0.43	0.03	0.01
STEEL	0.11	0.13	-0.44	-0.11

3.5.4 Conclusion

The results show that changes in the angle of incidence of lighting has a significant effect on the accuracy of the optical strain gauge. In view of the fact that the surfaces of the objects have relatively large asperities when viewed at the magnification of the apparatus, these results are to be expected. It can be concluded that the best accuracy can be attained when the lighting is coaxial with the optical axis of the system. Not only does

this provide a constant angle of incidence but it will also have the effect that surface features will be much better defined. This is because asperities will no longer appear as three-dimensional features with shadows that may change the appearance and location of the features as the angle of incidence of the light is changed.

3.6 Optimization of Lighting

3.6.1 Introduction

The experimental apparatus has provisions to effect coaxial lighting. It consists of a "T" junction in the optical tube just behind the focal lens, into which a light source can be introduced. The light is then reflected 90° coaxially and integral with the optical system by means of a semi transparent mirror installed at a 45° angle inside the optical tube.

Trials were conducted in this configuration with 30-inch goose neck fiber optic light transmitters whose polished ends were inserted into the T-junctions. The light sources were Fostec DCR IIs' equipped with EKE quartz halogen lamps and detachable infrared filters. However, these tests were not successful since the available light source was of insufficient intensity and did not illuminate the specimen surface adequately to obtain images. The explanation is that the 45° angle mirror is semi transparent and only a portion of the light gets reflected onto the object surface, resulting in the illumination to

be inadequate. It is concluded that a much stronger light source or a different optical arrangement would be required for this configuration.

Since a stronger light source was not available for the experiments, another, practicable solution had to be found for the lighting requirements of the subsequent experimental work. The best alternative was the external installation of the light source at the possibly most parallel angle relative to the optical axis.

It was possible to effect such a configuration by attaching the polished ends of the fiber optic conductors next to each of the two objective prisms at an angle of 15° relative to the optical axis. The lights were installed in such a way that the respective areas of the surfaces to be photographed were in the center of the light spots when the images were in focus. This configuration provides approximately 15 mm diameter circular light spots on the object's surface. Since this configuration is an integral part of the apparatus, it facilitates a constant angle of incidence of the light, and consistent lighting of the object's surface regardless of position or the rotation of the apparatus.

The installation is illustrated in Figure 3.9. The light source was equipped with infrared filters which, in conjunction with the fiber optic light transmission, provided cold light, thus eliminating any thermal effect.



The figure shows the arrangement of the two fiberoptic spotlights. They are installed externally at an angle of 15° to the optical axis. The distance to the object is adjusted so that the location of the light spots is optimized when the surface is in focus.

Figure 3.9 Optical Lighting Arrangement

3.6.2 Tests

Because it was planned to use the spot light method for all subsequent test work, its performance and suitability needed to be evaluated. Therefore, a test series was conducted where the method was compared against the light bar method used previously. The parameters of interest were the system's accuracy .

3.6.2.1 Test procedure

The test procedure was similar to that carried out for the tests to evaluate the effect of the angle of incidence of light, however with the difference that only the illumination with the light bar positioned at 45° was compared with that of the spot lights. Four different materials were tested which are listed below:

granite
limestone
potash
aluminum

The accuracy of the system can be determined by repeated image acquisition of a constant, non-changing surface, and the determination of the amount of apparent displacement of surficial features in the different images relative to one another.

The amount of apparent displacement can then be considered a measure of the entire system's "noise". This can be a function of the quality of the acquired image, variations in the performance of the system's hardware components such as lighting, the cameras and the image digitization and storage, and lastly the performance of the image analysis method.

Changes in environmental conditions such as vibration and variations in temperature also contribute to inaccuracies but they are external to the system and can therefore be

controlled during the performance of the tests. In the case of the present work, the experiments were carried out in an air-conditioned laboratory in a basement, and hence, the temperature was constant and there was no vibration.

The test series consisted of the following:

- acquisition of five sets of images (the set consisting of a reference camera #1 and camera #2 image and a secondary camera #1 and camera #2 image) of the specimen surface using the 45° light bar
- repetition of the same procedure using the spot lights
- determination of apparent displacement of surficial features for each set of images by template matching
- determination of averages and standard deviations of the apparent displacements
- comparison of the results of one set of experimental conditions with that of another set

The procedure was repeated for all materials listed above. The results are given below.

3.6.3 Results

In order to obtain a quantitative measure of the performance of the two configurations, the average values by which the apparent displacements deviate from zero can be used. However, in the experimental work these values are a combination of positive and

negative numbers, and the averages cannot be used as a true representation of the deviation since, in theory, it may be zero while the deviations may be large. Therefore, the standard deviations are used to arrive at a true indication of the apparent displacement of surficial features while the averages are observed to verify the absence of systematic errors or deviations from around zero.

The results are presented in the tables below. Table 3.6.1 shows the apparent displacements of surface features. The data are the averages and standard deviations for five tests. The results in the table show that in tests with all materials the spot lights gave lower standard deviations than the light bar. This is an indication that the surfaces were better illuminated with the spot lights, producing better images.

Table 3.6.1 Apparent X-Axis Displacement as a Function of Light Source
(averages and standard deviations for 5 tests)

Material	Camera #1				Camera #2			
	Spotlight (pixels)		Light Bar (pixels)		Spotlight (pixels)		Light Bar (pixels)	
	Avg.	Stdev.	Avg.	Stdev.	Avg.	Stdev.	Avg.	Stdev.
Aluminum	0.001	0.030	0.087	0.248	-0.088	0.030	0.023	0.104
Granite	0.012	0.020	-0.010	0.080	0.012	0.027	0.017	0.029
Limestone	0.013	0.017	-0.026	0.048	-0.008	0.033	0.004	0.038
Potash	0.047	0.075	-0.056	0.114	-0.040	0.045	-0.015	0.116

As already discussed previously, the deviation from zero is the "noise" or the accuracy of the system. When the X-axis displacement is calculated as apparent strains using equation 11, then the accuracy of the system can be expressed in μ -strains, which is listed in Table 3.6.2. The calculation is based on the experimental data shown in Table 3.6.1.

The results show again that the spot lights produce a better accuracy than the light bar, particularly in the case of aluminum and potash.

Table 3.6.2 X-Axis Displacement
Expressed in μ -strains

APPARENT STRAIN (X-axis)		
MATERIAL	μ -STRAINS	
	SPOTLIGHT	LIGHT BAR
ALUMINUM	+/-1.1	+/-3.9
GRANITE	+/-1.0	+/-1.1
LIMESTONE	+/-1.2	+/-1.4
POTASH	+/-1.7	+/-4.3

3.7 Optimization of Camera Performance

As mentioned above, the system's noise is a function of the sum of the performances of the various components comprising the system.

The most important parameter is the measurement of the relative displacements of features on the two images of the test surface separated from one another by a known, constant distance. In the configuration used in the experimental apparatus the images are acquired by two separate cameras held in place mechanically so as to ascertain that the distance between them is constant.

However, regular CCD camera images are to varying degrees subject to float, jitter and compression variations, showing on the screen as movement of the image, and also manifesting itself as measurable displacement of the pixel locations.

When there are two separate cameras each with its own set of fluctuations, such as is the case with the experimental apparatus, the relative distance of surficial features between the two images will vary according to the degree of fluctuations, adversely affecting the accuracy of the displacement measurements. Using a single camera which is able, by means of a suitable optical prism, to generate a single split image of two separate areas can reduce this effect substantially, since the image variations will affect the split image more uniformly than that of two separate camera images.

During the initial experimental work it was noted that the images of both cameras showed discernible movement. It was found that one major parameter for the performance of a CCD camera is the supply of electrical power. CCD cameras are sensible to inductive noise such as that of electrical motors, etc. in the electrical lines. In the case of the experimental apparatus, a regular plug-in transformer & rectifier (Basler Electric Class 2 Plug-In Transformer) was used to convert the 110VAC line voltage to 24 VDC needed for the cameras. This was found to be the primary reason for the relatively high variation of the optical sensor system experienced in some of the initial work with the apparatus.

3.7.1 Tests on the effect of power supply on the performance of CCD cameras

To study how the type of power supply affects the movement of the camera image, the Basler Electric Class 2 Plug-In Transformer (hereon in referred to as “plug-in”) power supply was compared with power obtained from two 12V (car) batteries connected in series, giving a constant power of 25 VDC. Tests were conducted with the optical apparatus and the template matching program to quantify the performance.

The following test procedure was employed:

- using the plug-in power supply, acquisition of eight successive sets of images (the set consisting of a reference camera #1 and #2 image and a secondary camera #1 and #2 image) of a stationary aluminum specimen surface, using the spot lights
- repetition of the same procedure with the battery system.
- determination of apparent displacement of surficial features for each set of images by template matching.
- determination of averages and standard deviations of the apparent displacements.
- comparison of the results of one set of experimental conditions with that of the other set

3.7.2 Test results

The effect of the type of power supply on the movement of the images is shown in Table 3.7.1 and Figure 3.10. It can be seen that the type of power supply has a significant effect on the performance of the CCD camera.

Table 3.7.1 Effect of Power Supply on the Movement of the Camera Images

sample number	movement of images (pixels)			
	battery image camera #1	battery image camera #2	plug-in image camera #1	plug-in image camera #2
1	0.02	0.03	-0.01	-0.27
2	0.07	-0.01	-0.05	0.00
3	-0.06	0.01	0.24	0.19
4	-0.02	0.02	-0.23	0.03
5	-0.01	-0.01	0.14	-0.22
6	0.02	0.00	0.10	0.00
7	0.01	0.03	-0.07	0.15
8	-0.04	-0.02	-0.09	0.19

As shown in the table, and in figure 3.10, the X-axis movement of the images can be as high as 0.24 pixels and 0.27 pixels respectively for images #1 and #2 when the plug-in power supply is used. In contrast, image movement with the battery power supply show maximum variations of 0.07 and 0.03 pixels for images #1 and #2 respectively, well below the nominal pixel resolution of 0.125.

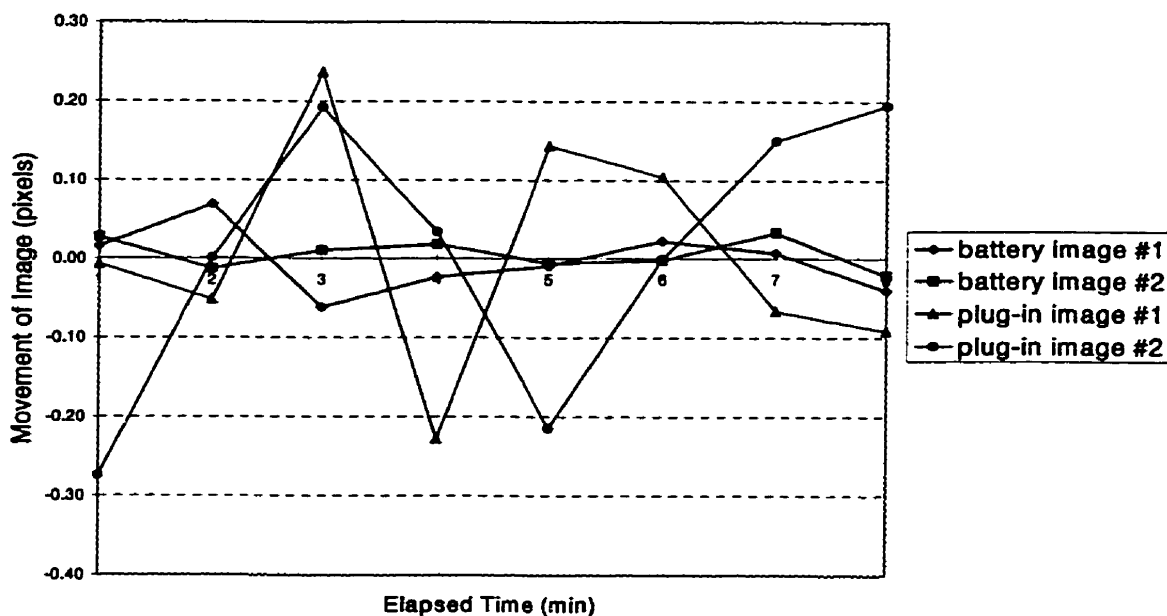


Figure 3.10 Effect of power supply on image movement

When these variations are converted into apparent strains using equation 11, the results obtained are given in Table 3.7.2 and Figure 3.11. In this case, the difference in performance for the two different configurations becomes even more conspicuous. The tests with the plug-in power supply resulted in a peak apparent deviation of 15.77μ -strains, almost twice that of the nominal resolution of 9.43μ -strains, while with the battery as power supply the maximum apparent deviation was 2.31μ -strains. It will be noted that apparent displacements are sometimes below the nominal resolution of the apparatus and should, in theory, be impossible to obtain. However, due to the statistical procedure in calculating $\delta X1$ and $\delta X2$ it is possible to get values which are lower than the nominal resolution. Therefore, these values should be considered zero.

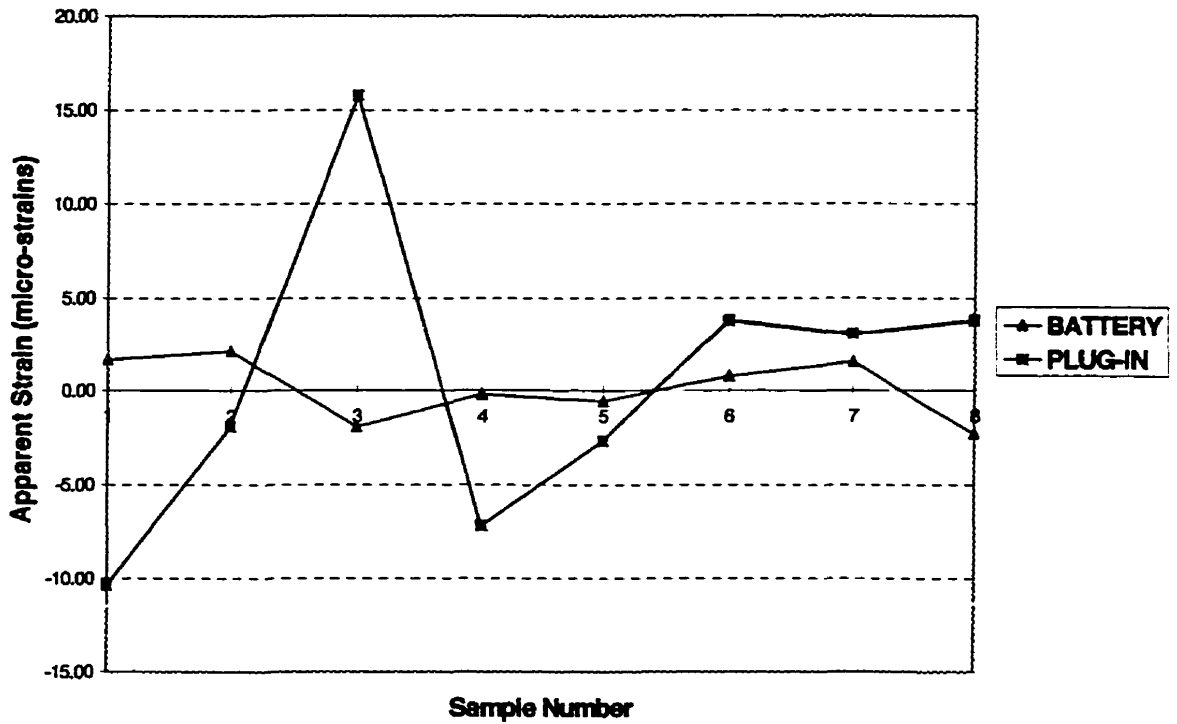


Figure 3.11 Effect of power supply on apparent strain

Table 3.7.2 Effect of Power Supply on Apparent Strain

sample number	μ-strains	
	battery	plug-in
1	1.60	-10.40
2	2.07	-1.92
3	-1.94	15.77
4	-0.22	-7.21
5	-0.59	-2.68
6	0.74	3.76
7	1.50	3.03
8	-2.31	3.76

3.7.3 Conclusions

As mentioned earlier, the effect of movement of the images is reduced substantially when a single camera is used, something which should be considered in the commercial development of an optical sensor. However, the experimental apparatus is equipped with two cameras, and the image movement is a detriment in the performance of the tests for the validation of the measuring principle. It was therefore fortunate that the problem could be identified, and that a satisfactory solution could be found.

Since the variance of the image movement, and also the total accuracy of the system in the tests with the battery was found to meet the desired criteria of the apparatus, it was decided that all further tests will be carried out with the battery system as power supply for the cameras.

In view of the fact that previous work on the determination of the image size and the effect of angle of incidence of lighting was carried out with the plug-in power supply, the validity of these results was re-examined in light of the low accuracy obtainable with this device.

The least significant effect of the lack of accuracy is in the determination of the image size. The micrometer with a precision of $25.4 \mu\text{m}$ was used to calibrate this size. At an accuracy of ± 0.25 pixels such as obtained with the plug-in power supply, the optical

sensor is considerably more accurate than the micrometer. Therefore, the calibration remains valid.

In tests for the effect of the angle of incidence of lighting, the low accuracy of the system can be disregarded since the test did not include an absolute measurement but was a qualitative and relative comparison. In addition, it involved the taking of five samples in each test for which standard deviations were determined. Hence, any unusual random deviation would have had only a small effect on the final result.

CHAPTER 4: VALIDATION OF THE OPTICAL-DIGITAL SENSOR AS A STRAIN GAUGE

4.1 Introduction

The ultimate purpose of the experimental work is to validate the optical-digital method as a means to measure strains such as used in the measurement of material properties and stresses. In effect, the work sets out to show that the method performs equally to that of the conventional methods used, but with a major advantage that there is no need for contact with the surfaces to be measured.

In order to demonstrate the validity of the novel method, a series of tests was conducted.

The objective of the tests was to

- directly compare the strain measurement by the optical strain gauge to that of electrical strain gauges
- to conduct these measurements with a method that is valid and accepted in the domain of materials testing so as to prove the performance and the validity of the optical sensor
- to see how the surface appearance and morphology of different materials affects the performance of the method

4.2 Experimental Methodology

4.2.1 Test set-up and procedure

The measurement of the deformability parameters of a material like rock involves the placement of a sample, usually in the shape of a cylindrical rod with a length to diameter ratio of about 2:1, in a press and applying pressure onto the sample to attain axial and transversal strains. The amount of axial and transversal strain, in the range of μ -strains, is normally measured by strain gauges attached axially and transversely onto the side of the sample. The amount of strain at a given load is used to calculate the elastic modulus E and the Poisson's ratio ν of the material respectively. This is an ASTM standard procedure described as D-3148-86 in the ASTM standard test methods.

In the case of the experiments, the test samples consisted of diamond drill cores and machined rods respectively, with a diameter of 100 mm and a L/D ratio of 2.0. The following materials were tested:

granite
limestone
potash
aluminum

Electrical 15 mm long 3-gauge rosette strain gauges of the type MM WK-13-500WR-350 with the gauges arranged at 45° from one another were used to measure the strains. The

gauges were used in conjunction with a Measurement Group SB-10 Balancing unit and a P 3500 Strain Indicator. Three strain rosettes were attached on the sides of each test specimens equi-distant from each end of the cylinder and equi-distant from one another around the perimeter of the specimen, with one gauge parallel, one at 45° and one perpendicular to the axis of the specimen. Owing to difficulties in attaining good bonding, the potash specimen had only one rosette installed.

The approved procedure was employed to glue the strain gauges onto the specimen, including preparation of the surfaces and using M-Bond AE-10 adhesive for the potash sample and M-Bond 200 adhesive for the remainder of the samples. For the purpose of identification of the electrical strain gauge and its orientation, the gauges were numbered as follows:

<u>Rosette #1</u>	axial gauge	#1
	45° gauge	#2
	transverse gauge	#3
<u>Rosette #2</u>	axial gauge	#4
	45° gage	#5
	transverse gauge	#6
<u>Rosette #3</u>	axial gauge	#7
	45° gage	#8
	transverse gauge	#9

The test samples were placed upright in a Tinius Olson 27 240 kg (60 000 pounds) capacity press and adjusted so that the applied compressive load would result in equal strain readings for all three axial strain gauges. Because of imperfections of the specimen ends and also because of inhomogeneity and anisotropy of some materials, this could be achieved only to varying degrees of success. The specimen were then loaded to 27 240 kg

(potash to 5 448 kg) and the load was decreased at increments of 4 540 kg (10 000 lbs) with potash at 908 kg (2 000 lbs), while taking strain gauge readings at each increment.

There were reasons for using a decreasing load cycle. The first reason was that it made it possible to verify the proper placement of the specimen. To do this, the strains of the three axial strain gauge readings were compared at maximum load and adjustments were made to the specimen in order to obtain reasonable agreement between the strain readings at the maximum loads. The other reason was that the specimen underwent large, non-linear axial translations in the direction of the applied load at the lower load increments due to settling-in of the specimen and flexion of the press platform (these became considerably smaller and more linear at higher loads). This had the effect that the optical strain gauge images showed large displacements at low loads. It not only adversely affected the accuracy of the measurement but also caused large portions of the surface features to be displaced beyond the image boundaries as the load was increased, making template matching virtually impossible.

The optical strain gauge was installed on the test machine table so that it was possible to photograph the specimen surface immediately next to one or between two of the rosettes.

As described in Section 3.2.1, the experimental apparatus is equipped with a feature that allows it to be rotated parallel with, and along the center of the optical axes of both camera systems, thus making it possible to measure strains on the specimen surface at any angle

(see Figure 3.5). This allows the strain measurement parallel to and perpendicular with the specimen axis as well as at 45° to the axis, similar to that of the strain rosettes.

Prior to a test, therefore, the optical strain gauge is rotated to the desired angle, the x-axis micrometer is used to search areas on the surface which have good contrast features, and the y-axis micrometer is used to bring the images into focus. Photographs are recorded at each load increment concurrently with the recording of the strains measured with the electrical strain gauge. The photographs are digitized, stored in a computer and processed by the method already described.

4.2.2 Image processing

Figure 4.1 shows typical surface images of the various materials. It can be seen that, in general, the images have poor contrast and seem out of focus. The reason for this is that the material surfaces are not polished but are the result of diamond drilling and machining the rock and aluminum sample respectively, resulting in relatively rough surfaces with large asperities when viewed at the magnification of the apparatus.

It was found that the lack of contrast was reflected in the accuracy of the results of the template matching procedure. As explained in Section 3.2.2, the procedure results in sets of 15 X- and Y-axis pixel displacement values (δX and δY) for each of the images which,

when viewed statistically, are a measure of how well the procedure was able to recognize and determine the location of each template. It can be seen in Figure 4.1 that the image of aluminum is the brightest, shows the most details and has good feature contrast. This is reflected in tests with aluminum where template matching typically resulted in low standard deviations. In contrast, the image of potash is almost devoid of features, having the effect that standard deviations are more than an order of magnitude higher than those of aluminum. The images of granite and limestone show features which the image processing procedure was able to recognize relatively well, resulting in standard deviations which were much better than that of potash. To illustrate this, the following table shows examples of strain measurement results and standard deviations obtained with the various core samples when subjected to an axial stress of 5.78 Mpa.

Table 4.2.1 Typical axial displacement results and standard deviations using the optical strain gauge and template matching procedure for core samples subjected to 5.78 Mpa stress

material	displacement $D_{x1}-D_{x2}$ @ 5.78 Mpa (μm)	standard deviation (μm)
Aluminum	2.243	0.063
Granite	3.257	0.319
Limestone	3.231	0.210
Potash	4.943	1.071

The examples indicate that the accuracy of the optical strain gauge method is to a large degree dependent on the quality of the images, which in the case of the experimental apparatus are poor, as seen in Figure 4.1. However, it must be kept in mind that these images were obtained with the experimental apparatus which has limited capabilities and



Figure a: aluminum



Figure c: limestone

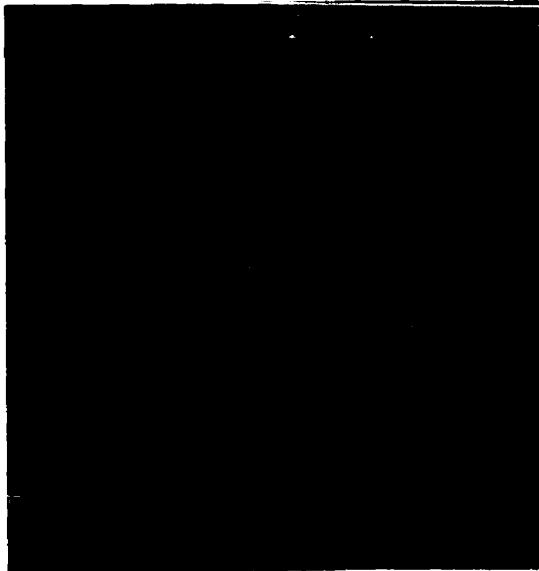


Figure b: granite

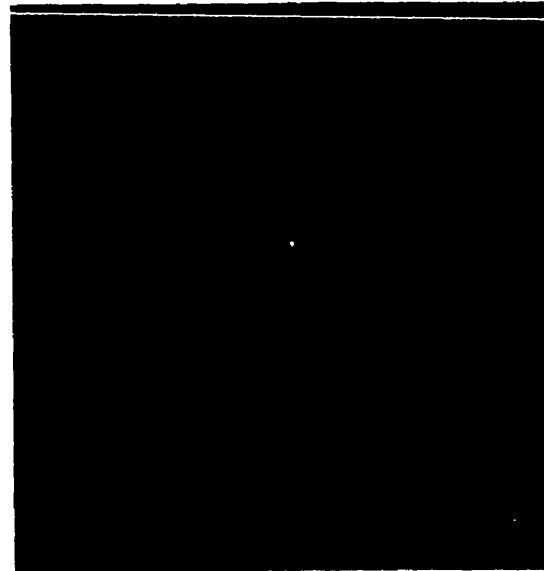


Figure d: potash

Figure 4.1
Typical Optical Strain Gauge Images of the Various Materials

is not able to produce better quality images. It is certain that an optimized system with coaxial lighting, better optics and a more suitable camera system will produce more consistent and better quality images, resulting in much better accuracies.

Another aspect of the experimental procedure is the relation between large axial translations of the images due to movement of the test specimen in response to the applied load and the small displacements of image features due to strain, which, on average was about 1/10 that of the axial translation. This certainly has a detrimental effect on the accuracy of the results.

Yet another aspect of the method is the template matching procedure which is probably not the best method available. It is certain that research and development for the optimization of the image recognition & position determination will produce a more robust software which will be capable of producing more accurate results.

With regard to axial rotation, the I1 and I2 Y-axis displacements in all tests were compared to verify the absence of divergence. It was found that all tests had virtually similar I1 and I2 Y-axis displacements with the largest difference found in a test with granite where the strain attributable to axial rotation was 0.1% that of the total strain.

4.3 Axial Strain Measurements

In the axial strain measurements, parallel with the applied load, the optical sensor was in a vertical position, and the measurements were compared with measurements made with the axial strain gauges #1, #4 and #7 respectively.

In the details below, the location and position of the optical sensor for each test is given in order to be able to evaluate the performance of the optical sensor by comparison with the corresponding strain gauges.

4.3.1. Aluminum

The initial tests were carried out with aluminum following the procedure outlined in Section 4.2.1.. Since aluminum is homogeneous and isotropic, it was reasonable to assume that the strains around the specimen would be relatively constant and that a direct comparison between the two sensing methods could be made.

The aluminum test specimen was positioned in such a way that the optical strain gauge photographed a region 10 mm next to and parallel with the axial gauge #4. It was hoped that the close proximity to the strain gauge would allow a direct comparison of the measurements between gauge #4 and the optical strain gauge.

The results are given in Table 4.3.1 and are shown in Figure 4.2 which also shows the theoretical values for aluminum based on a quoted elastic modulus of 10.6×10^6 psi (Marks Standard Handbook for Mechanical Engineers, see reference).

Table 4.3.1 Axial Strain Measurement of Aluminum (1)

Stress (MPa)	μ -strains		
	gauge #4	gauge #1	optical gauge
0	0	0	0
5.78	50	70	57
11.56	122	137	124.9
17.34	199	205	202.1
23.12	279	276	284.4
28.9	361	352	370.8
34.68	445	425	458.4

1. Optical sensor vertical 10 mm from gauge #4, between gauge #4 and gauge #1

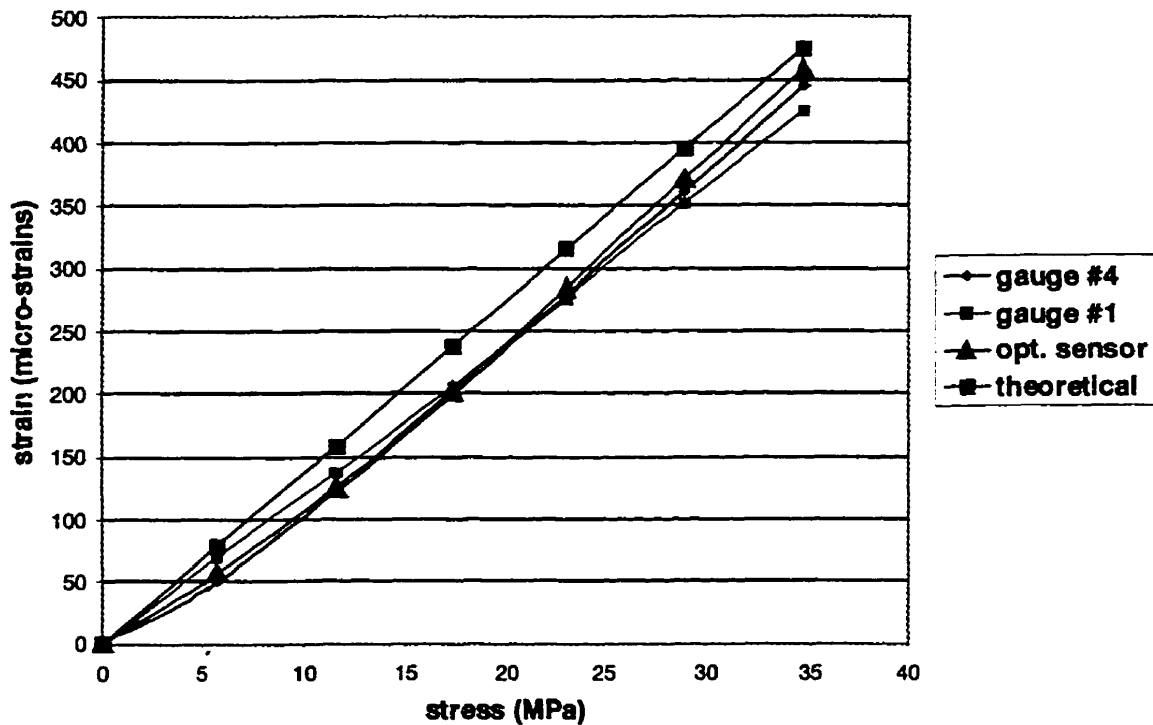


Figure 4.2 Axial strain measurement of aluminum
Optical sensor vertical 10 mm from gauge #4, between gauge #4 and gauge #1

The results show that the optical strain gauge follows very closely the axial strains measured with the electrical strain gauges. In addition, the optical gauge results compare more favorably with the theoretical curve than that of the electrical gauges.

In view of the successful result, the axial strain measurement comparison test was repeated with all other materials as detailed in the following section.

4.3.2 Axial strain measurements with other materials

The remainder of the materials, already listed previously, was subjected to the same axial tests as that with aluminum. The objective of the tests was to evaluate the optical strain measurement method with materials that have different mechanical properties and surface appearances such as seen in the field of mining and civil engineering.

The test procedure, described in Section 4.2.1, was similar to that for aluminum except for potash, where the load was only 5 448 kg instead of 27 240 kg. The results of the tests are given in Tables 4.3.2 to 4.3.4 and Figures 4.3a to 4.3c respectively.

It can be seen that for tests with granite, limestone and potash the results of the optical strain gauge are virtually identical with that of the respective electrical strain gauges. The slight differences between the strain measurement results are most likely attributable

Table 4.3.2 Axial Strain Measurements of Granite (1)

stress MPa	μ -strains		
	gauge #1	gauge #4	optical gauge
0	0	0	0
5.78	388	353	378.5
11.56	637	613	642.9
17.34	826	815	853.2
23.12	982	984	1019.8
28.9	1119	1131	1188.8
34.68	1256	1253	1316.2

1. Optical sensor vertically centered between gauges #1 and #4

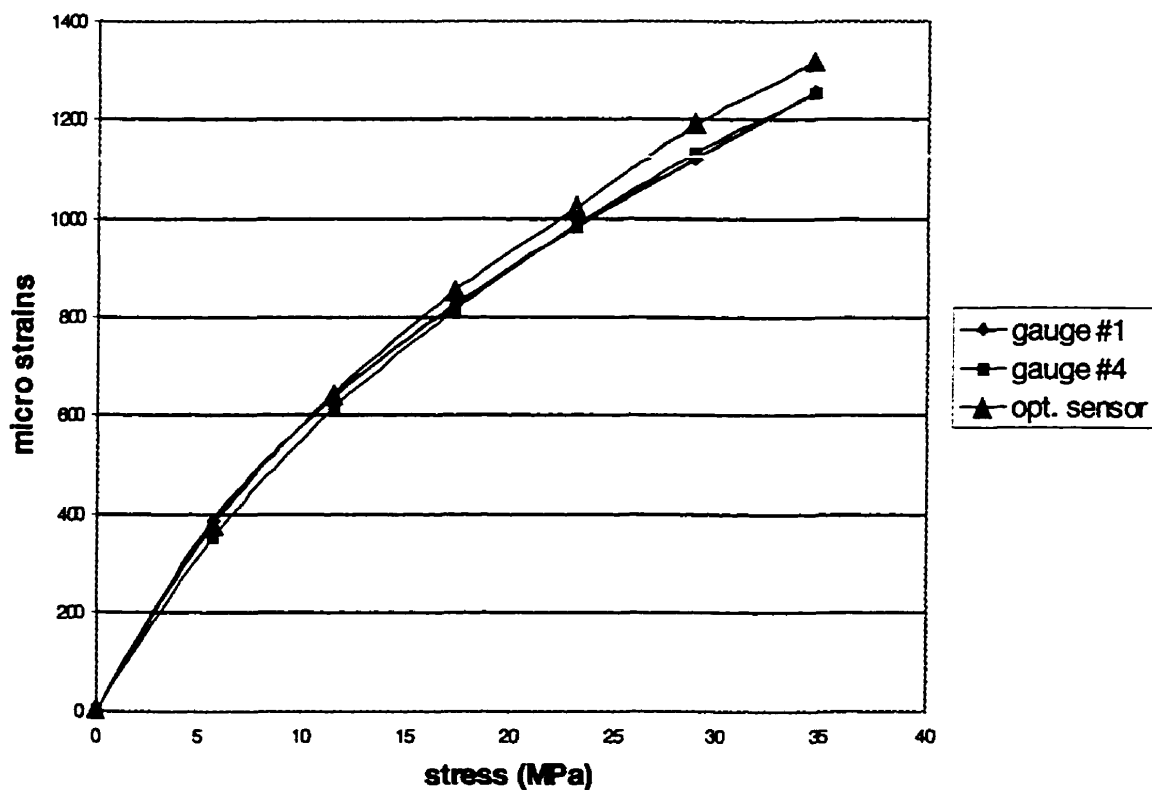


Figure 4.3a Axial strain measurements of granite
Optical sensor vertically centered between gauges #1 and #4

Table 4.3.3 Axial Strain Measurements of Limestone (1)

stress MPa	μ -strains		
	gauge #1	gauge #4	optical gauge
0	na	0.0	0
5.78	na	118.0	118.92
11.56	na	240.0	240.59
17.34	na	359.0	364.25
23.12	na	478.0	495.19
28.9	na	594.0	614.08
34.68	na	717.0	740.08

1. Optical sensor vertically next to gauges #4

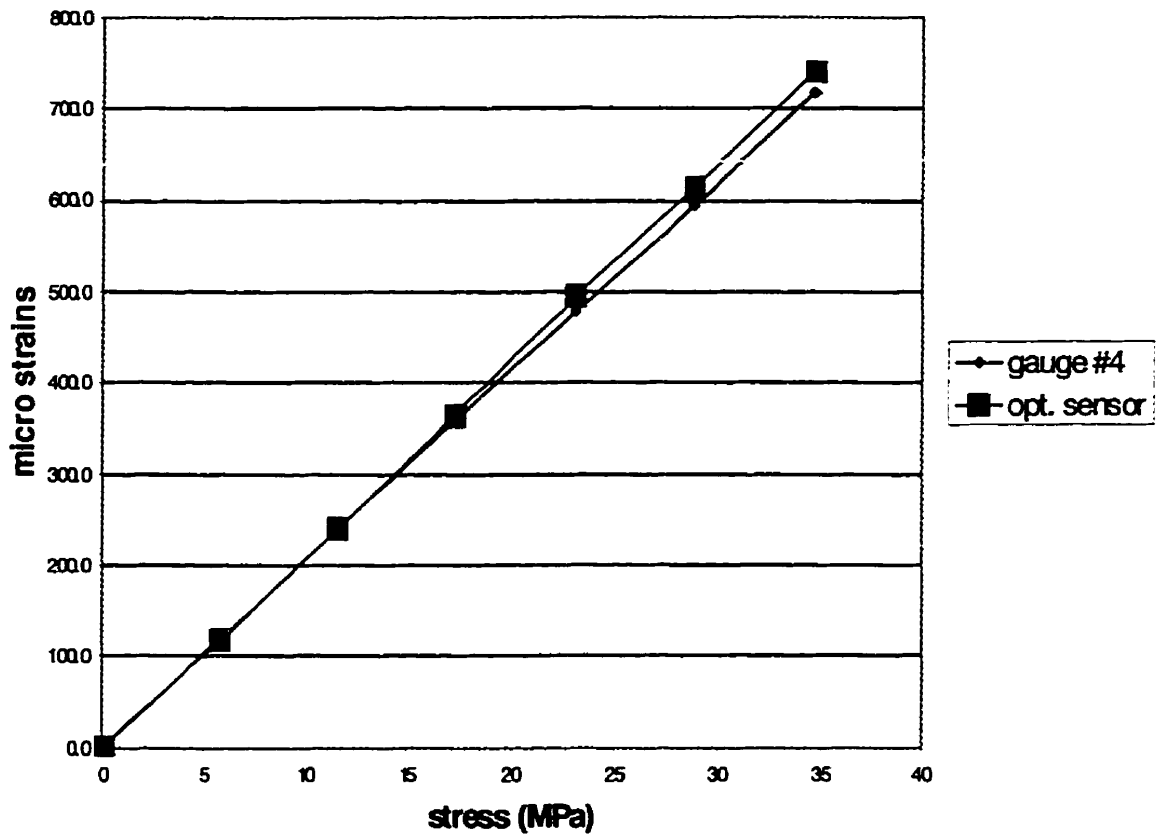


Figure 4.3b Axial strain measurements of limestone
Optical sensor vertically next to gauges #4

Table 4.3.4 Axial Strain Measurements of Potash (1)

stress MPa	μ -strains		
	gauge #1	gauge #4	optical gauge
0.00	0	na	0
1.16	134	na	158.2
2.31	185	na	207
3.47	230	na	254.8
4.62	272	na	300.9
5.78	312	na	348.8
6.94	352	na	388.2

1. Optical sensor vertically next to gauge #1

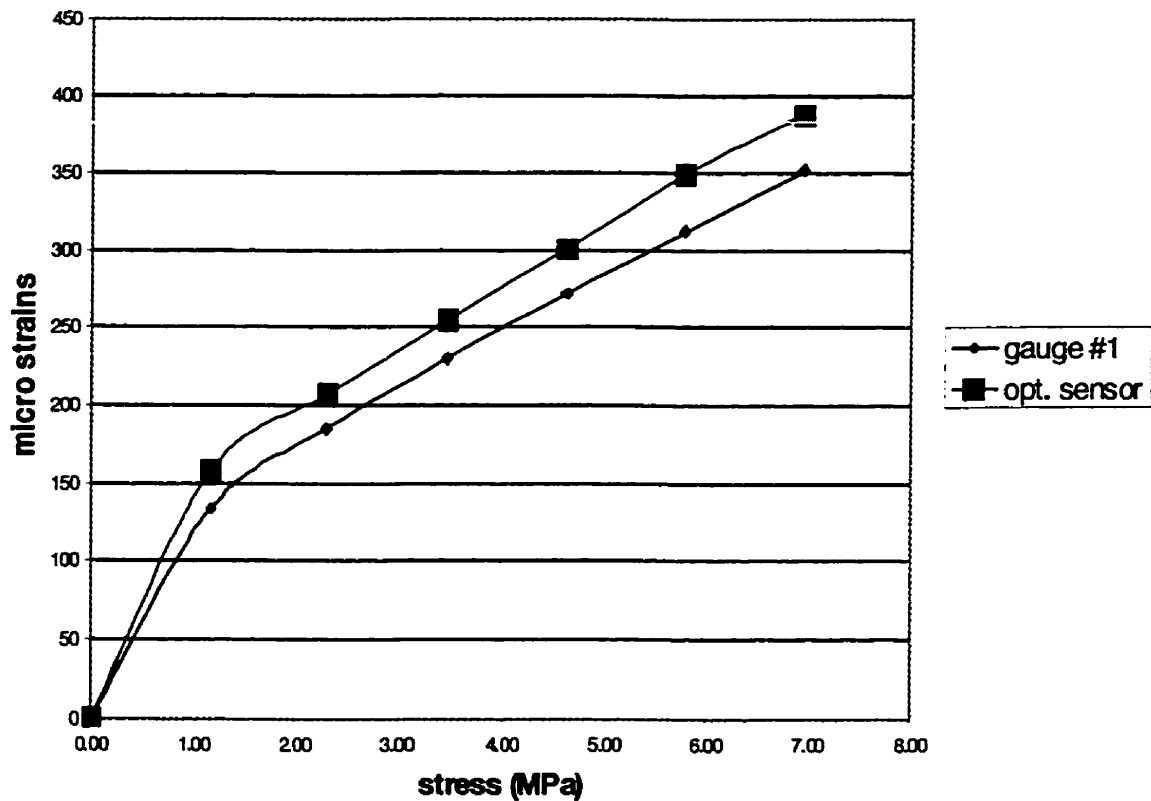


Figure 4.3c Axial strain measurements of potash
Optical sensor vertically next to gauge #1

to the fact that the optical strain gauge was not measuring in the exact same location as the comparative electrical strain gauge, and that actual strains on different locations of the specimen surfaces were not identical. The results are particularly remarkable for the test with potash and limestone, where the surface images did not show many distinguishing features and template matching results for both materials had relatively large standard deviations. It is also noteworthy that all results were obtained in spite of the large translations of the test specimen in the direction of the applied load.

4.4 Strain Measurements at other Angles

The objective of the following two test series was to see if the experimental apparatus would be capable of measuring strains at angles other than that of the specimen axis when subjected to axial loads so as to simulate the configuration of a rosette strain gauge.

The test series comprised measurements with the apparatus rotated at an angle of 45° , parallel with the 45° strain gauges #2, #5 and #8 respectively, and the apparatus rotated into a horizontal position to measure strains perpendicular to the applied load, parallel with strain gauges #3, #6 and #9.

Details of the tests are given in the following sections.

4.4.1 Strain measurements at 45° to the applied load

The results of the tests are given in Tables 4.4.1 to 4.4.4 and Figures 4.4a to 4.4.d respectively, and are discussed below. The figures show the comparison between strains measured with the optical strain gauge and the electrical strain gauges between which the optical measurements are made.

One factor in common for all tests with the optical strain gauge at 45° was that the measurements were erratic. A possible reason for the erratic results is that displacements attributable to the strains at 45° to the axis of the core are significantly smaller than the displacements caused by the translation of the core in the direction of the load. These large displacements may lead to higher inaccuracies in determining the template coordinates. This is supported by the observation that the results are more erratic at the lower load increments where the axial translation of the core sample is much higher than at the higher loads.

The test with aluminum at 45° includes the theoretical values for aluminum based on a quoted elastic modulus of 10.6×10^6 psi and a Poisson's Ratio of 0.33 (Marks' Standard Handbook for Mechanical Engineers). The results in Figure 4.4a show that, albeit very erratic, the optical sensor values follow the theoretical curve much closer than either of the electrical strain gauge. In addition it can be seen that the electrical strain gauge curves also show a certain degree of erratic behavior. The reason for this is not clear.

Table 4.4.1 Aluminum: strain measurement at 45° to the applied load(1)

stress MPa	μ -strains		
	gauge #5	gauge #2	optical gauge
0	0	0	0
5.78	15	7	51.6
11.56	35	17	62.3
17.34	57	28	100.3
23.12	80	40	117.2
28.9	104	52	143.3
34.68	145	81	184.4

1. Optical sensor at 45° 10 mm from gauge #5 between gauges #5 and #2

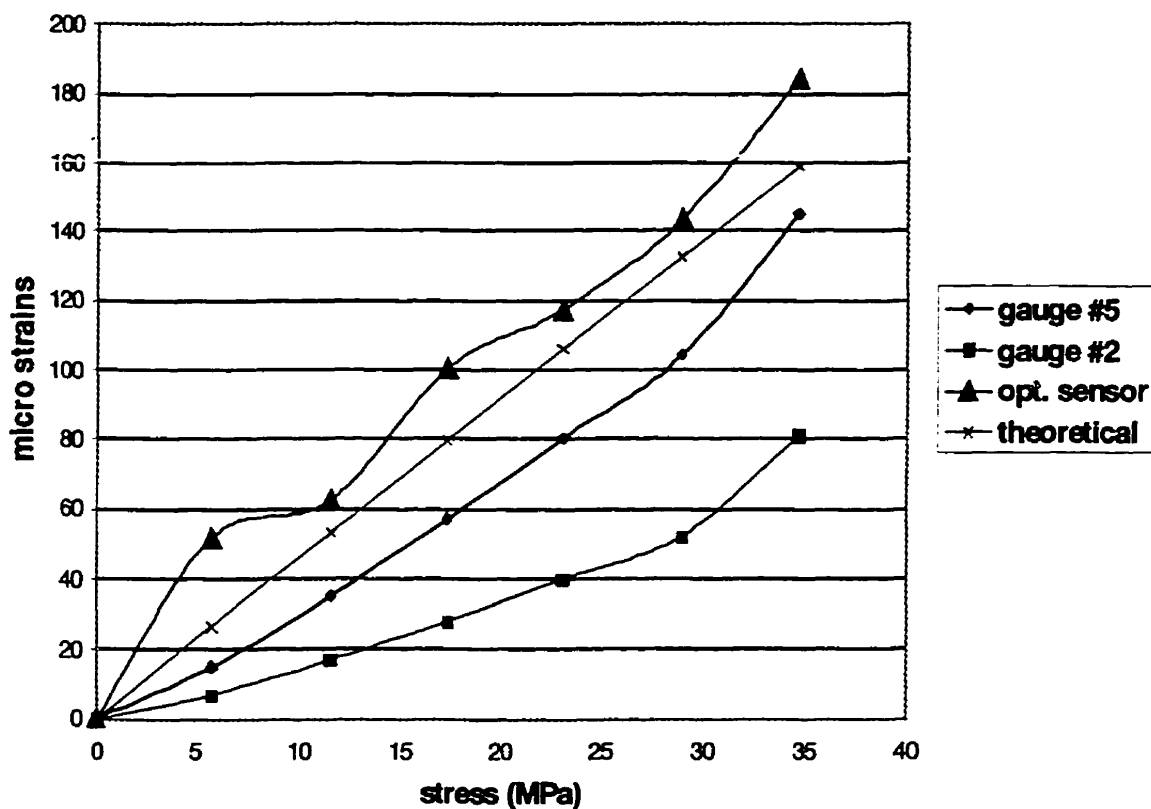


Figure 4.4a Aluminum: strain measurement at 45° to the applied load
Optical sensor at 45° 10 mm from gauge #5 between gauges #5 and #2

Table 4.4.2 Granite: strain measurement at 45° to the applied load(1)

stress MPa	μ -strains		
	gauge #2	gauge #5	optical gauge
0	0	0	0
5.78	121	133	176.6
11.56	202	214	289.1
17.34	269	268	374.7
23.12	305	315	446.6
28.9	347	355	534.6
34.68	399	426	626.6

1. Optical sensor at 45° centered between gauges #2 and #5

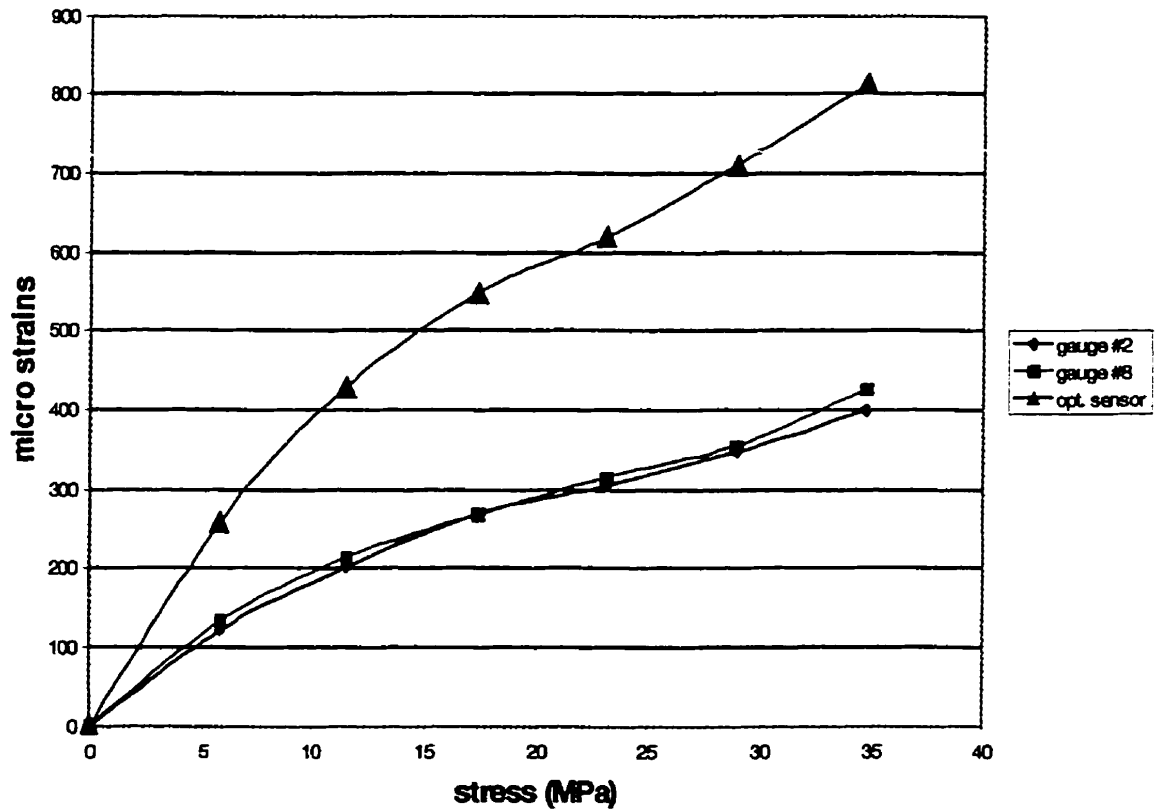


Figure 4.4b Granite: strain measurement at 45° to the applied load
Optical sensor at 45° centered between gauges #2 and #5

Table 4.4.3 Limestone: strain measurement at 45° to the applied load(1)

stress MPa	μ -strains		
	gauge #2	gauge #5	optical gauge
0	0	0	0
5.78	41	42	47.4
11.56	76	74	86.8
17.34	109	104	106.9
23.12	138	132	126
28.9	165	155	163
34.68	212	192	194.7

1. Optical sensor at 45° centered between gauges #5 and #2

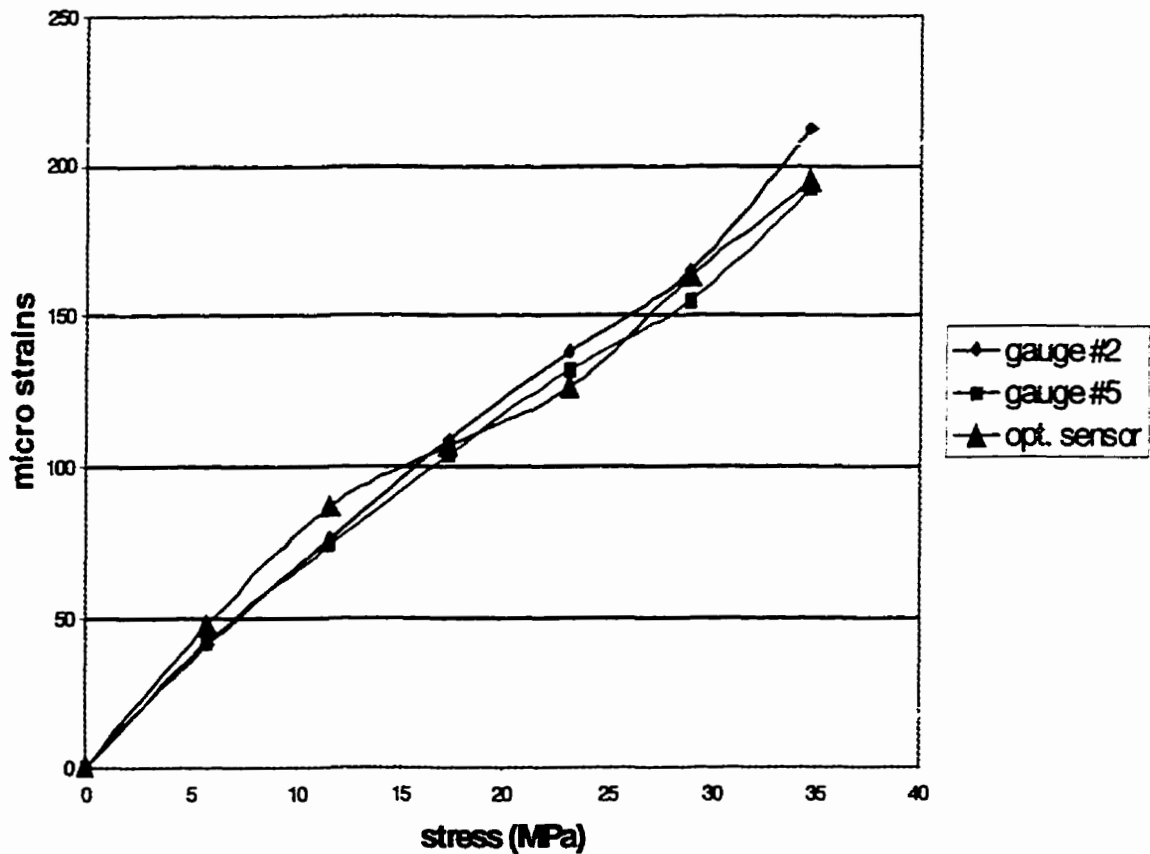


Figure 4.4 c Limestone: strain measurement at 45° to the applied load
Optical sensor at 45° centered between gauges #5 and #2

Table 4.4.4 Potash: strain measurement at 45° to the applied load(1)

stress MPa	μ-strains		
	gauge #2	na	optical gauge
0.00	0	na	0
1.16	7	na	77.9
2.31	10	na	82.8
3.47	16	na </td <td>96.3</td>	96.3
4.62	18	na	103.5
5.78	21	na	152.5
6.94	26	na	157.4

1. Optical sensor at 45° next to gauge #2

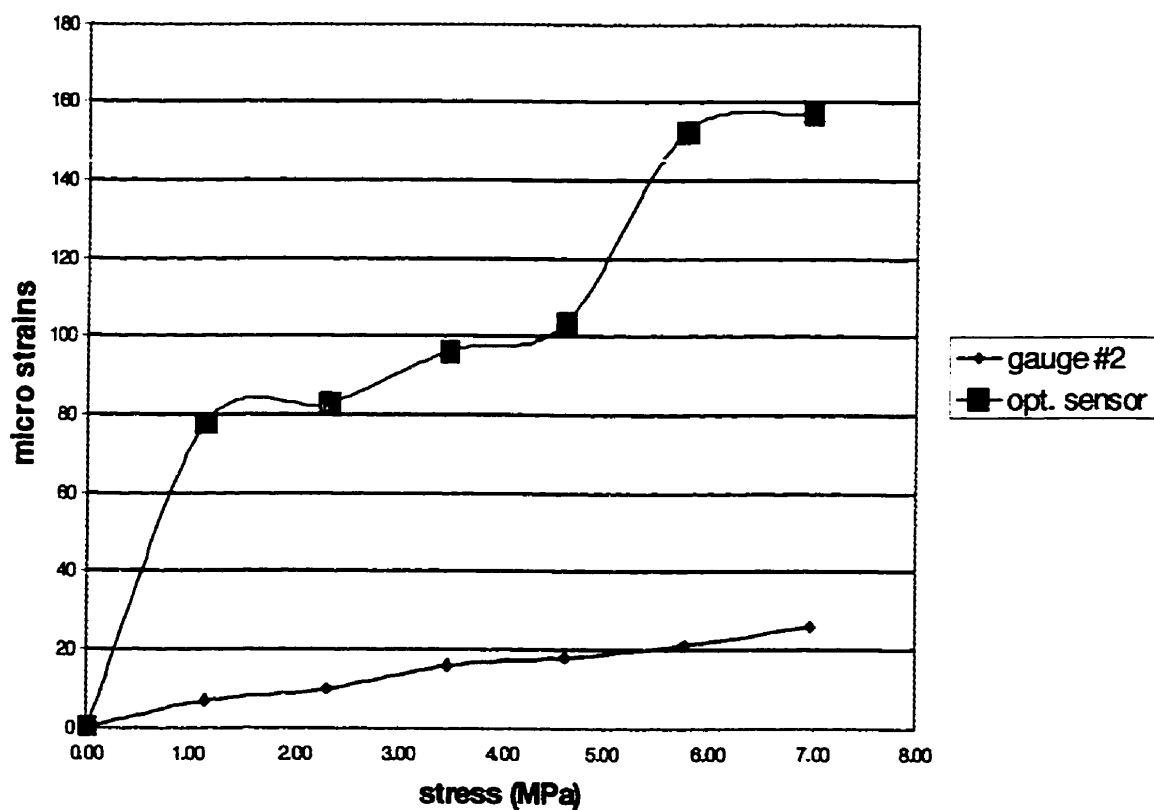


Figure 4.4d Potash: strain measurement at 45° to the applied load
Optical sensor at 45° next to gauge #2

In the test with granite the strain measurements with the optical strain gauge was generally higher than that of the corresponding electrical strain gauge, while there was good agreement between the optical strain gauge and both electrical strain gauges in the test with limestone. In the test with potash the optical strain gauge gave very erratic results without any correspondence with the electrical strain gauge.

4.4.2 Strain measurements normal to the load

In this test series the apparatus was rotated into a horizontal position to measure strains normal to the applied load, parallel with strain gauges #3, #6 and #9. The results of the tests are given in Tables 4.4.5 to 4.4.8 and Figures 4.4e to 4.4h respectively.

As can be seen in Figure 4.4e, in the aluminum test the optical sensor measurement follows closely that of the theoretical curve based on a Poisson's Ratio of 0.33 and that of gauge #6, 10mm next to the optical measurement location, albeit in an erratic manner. In the test with granite, the optical strain gauge was placed in the center between gauges #3 and #9. The measurements followed the general trend of the electrical strain gauges but was slightly lower than the readings of gauge #3 and considerably lower than gauge #9. The best results in the test series were obtained with the limestone specimen. The optical strain gauge was located in the center between the electrical strain gauges #3 and #6, and the optical strain curve was also between the curves of the two gauges.

Table 4.4.5 Aluminum: strains normal to the applied load (1)

stress MPa	μ -strains		
	gauge #6	gauge #3	optical gauge
0	0	0	0
5.78	19	36	28.2
11.56	47	70	60.6
17.34	78	107	81.2
23.12	110	143	115.4
28.9	143	182	137.7
34.68	175	223	169.3

1. Optical sensor horizontal 10 mm from gauge #6,
between gauge #6 and gauge #3

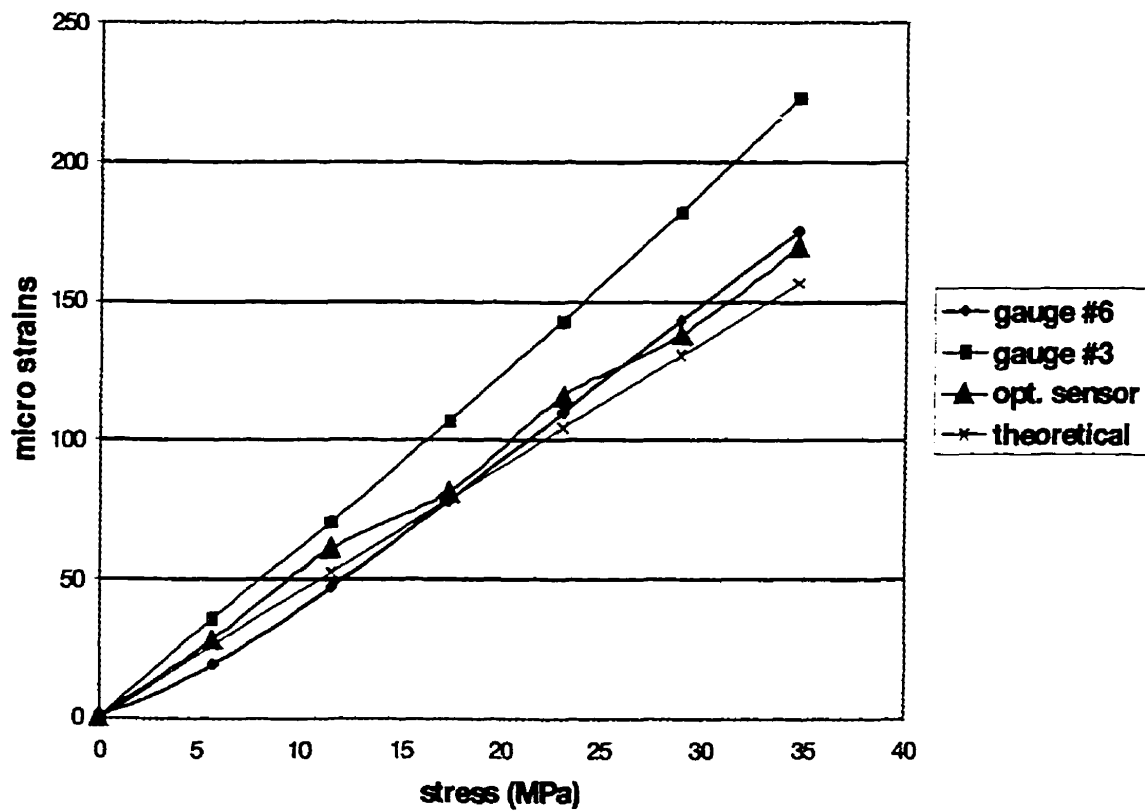


Figure 4.4e Aluminum: strains normal to the applied load
Optical sensor horizontal 10 mm from gauge #6, between gauge #6 and gauge #3

Table 4.4.6 Granite: strains normal to the applied load (1)

stress MPa	μ -strains		
	gauge #3	gauge #9	optical gauge
0	0	0	0
5.78	61	67	48.8
11.56	118	113	91.2
17.34	164	149	132.6
23.12	206	179	164.3
28.9	249	209	205.6
34.68	282	237	230.4

1. Optical sensor horizontal between gauge #3 and gauge #9

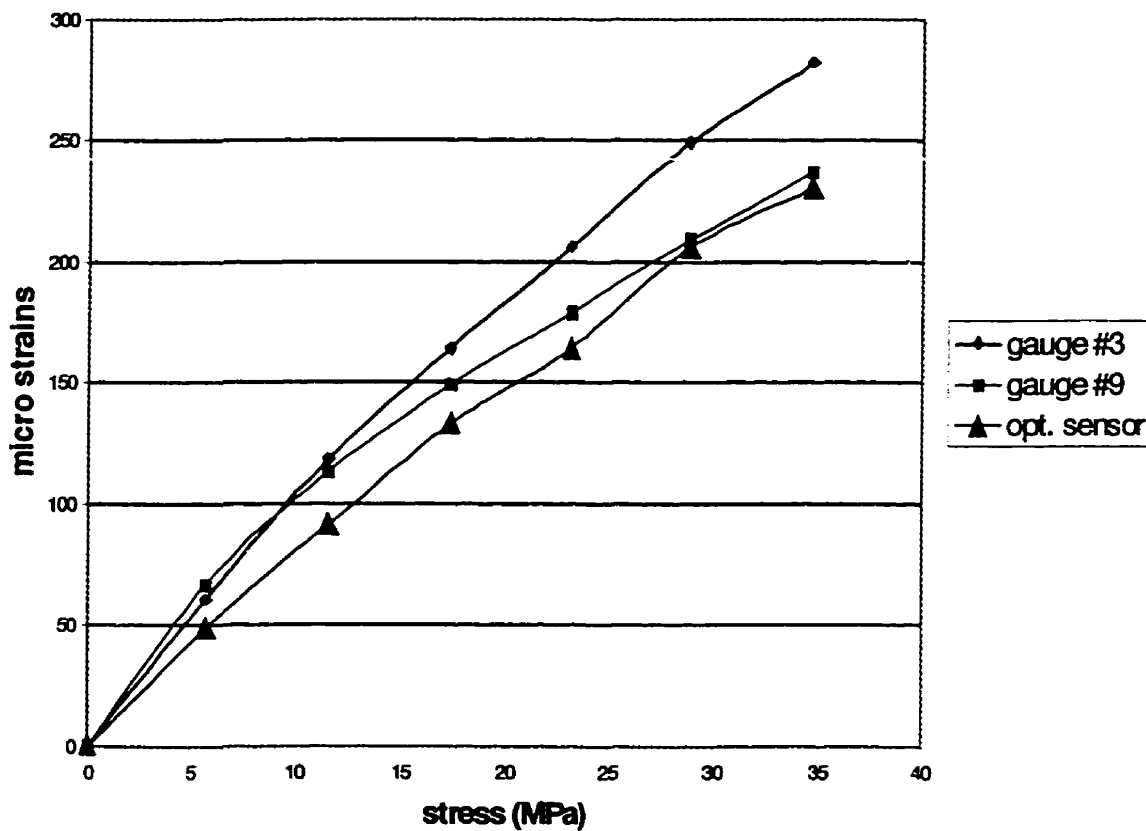


Figure 4.4f Granite: strains normal to the applied load
Optical sensor horizontal between gauge #3 and gauge #9

Table 4.4.7 Limestone: strains normal to the applied load (1)

stress MPa	μ -strains		
	gauge #3	gauge #6	optical gauge
0	0	0	0
5.78	36	39	33.3
11.56	70	81	69.1
17.34	103	123	113
23.12	136	168	148.9
28.9	170	214	194.4
34.68	196	257	242.1

1. Optical sensor horizontal between gauge #3 and gauge #6

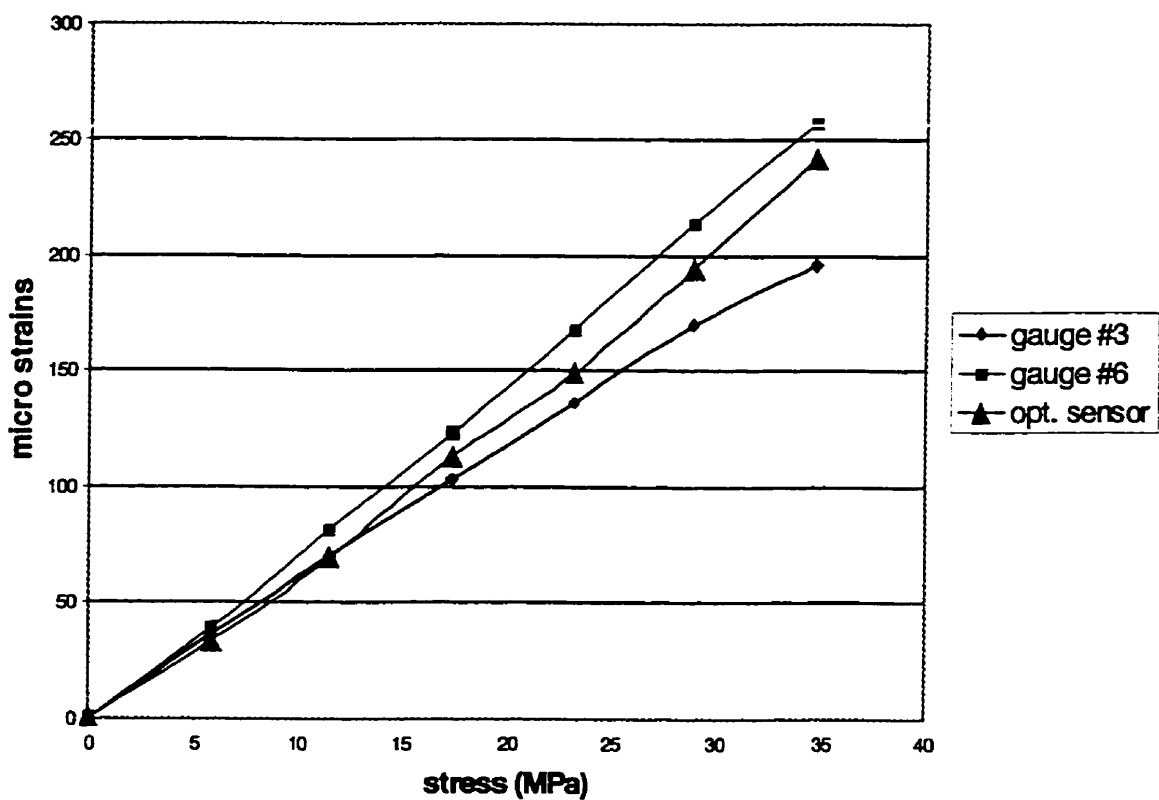


Figure 4.4g Limestone: strains normal to the applied load
Optical sensor horizontal between gauge #3 and gauge #6

Table 4.4.8 Potash: strains normal to the applied load (1)

stress MPa	μ -strains		
	gauge #3	na	optical gauge
0.00	0	na	0
1.16	30	na	92.3
2.31	52	na	112.7
3.47	70	na	141.8
4.62	86	na	166.9
5.78	101	na	188.6
6.94	114	na	205

1. Optical sensor horizontal 10 mm from gauge #3

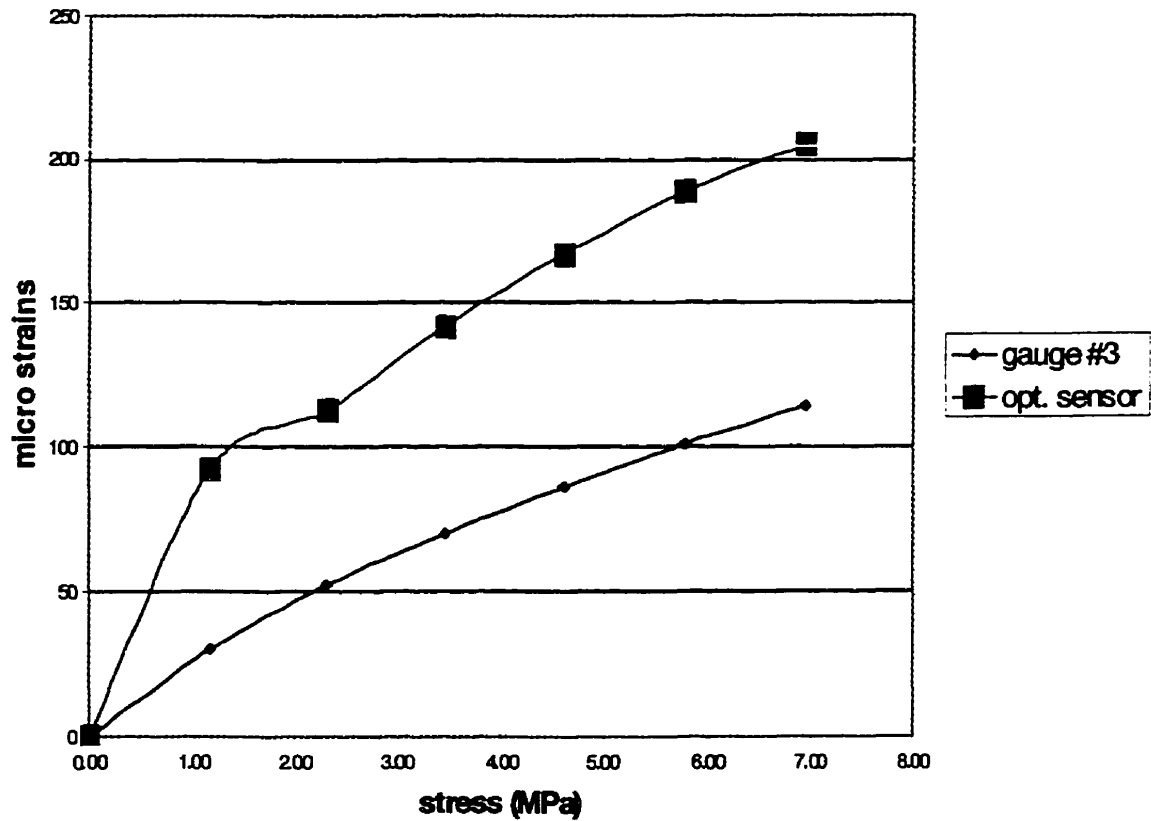


Figure 4.4h Potash: strains normal to the applied load
Optical sensor horizontal 10 mm from gauge #3

The test with potash was unstable at the low end of the load cycle while the remainder of the readings were stable but much higher than that of the electrical strain gauge. There was poor image quality in this test, which resulted in large standard deviations in the template matching results, and the necessity to eliminate a large number of coordinate values, particularly for values at the lower load increments where the large axial translation has a significant effect on the accuracy of the results.

CHAPTER 5: DISCUSSION

One way of demonstrating the validity of the digital image analysis method was to directly compare strain measurements of the optical strain gauge with that of electrical strain gauges in recognized and accepted tests such as the uniaxial load test used to determine the elastic properties of materials. However, before these tests could be conducted, the characteristics of the experimental apparatus needed to be established, and the different parameters affecting the quality of the measurements were identified and optimized.

Within this initial test work it was found that the angle of incidence of the light on the object had a significant effect on the accuracy of the strain measurements. In view of the fact that the surfaces of the objects have relatively large asperities when viewed at the magnification of the apparatus, this effect was to be expected. It was concluded that the best accuracy can be attained when the lighting is provided directly through the optical system coaxially with the optical axis. Not only does this provide a constant angle of incidence but it will also have the effect that surface features will be much better defined. This is because asperities will no longer appear as three-dimensional features with shadows that change the appearance and location of the features as the angle of incidence of the light is changed. Since coaxial lighting was not possible in the experimental work, a set of fiber optic spotlights, as described previously, was used. This set-up performed well enough to allow the performance of the experiments.

It was also observed that the images displayed a considerable amount of float and compression variations. Since the apparatus has two independent camera systems, each with its own set of fluctuations, it was found that this had a significant effect on the accuracy of the strain measurements. These fluctuations could be reduced by almost an order of magnitude by using a constant, noise-free power source such as that of a battery instead of a regular electrical line DC power supply. It should be possible to reduce the deleterious effect of image fluctuations further if a single camera system is used.

One of the objectives of the experimental work was to evaluate the effect of surface morphology on the accuracy of the strain measurements. It was found that surfaces with little details caused difficulties in properly locating templates. In tests with potash, for example, whose surface had an almost amorphous appearance, the rejection rate of template matching coordinates was much higher than that in other materials which had better surface definitions. This was also reflected in the experimental results, where potash usually showed a much lower correlation with the electrical strain gauges than that of other materials.

Experiments to validate the optical-digital method was designed not only to demonstrate the viability of the concept but also to evaluate its performance when used in a rosette strain gauge configuration. The objectives could be met by conducting uniaxial loading tests and comparing the measurements of the optical strain gauge with that of electrical rosette strain gauges at different angles relative to the direction of the load.

It was found that the optical strain gauge performed very well in axial strain measurements. In tests with aluminum, granite, limestone and potash the results of the optical strain gauge were virtually identical with that of the respective electrical strain gauges. Slight differences between the strain measurements were attributed to the fact that the optical strain gauge was not measuring at the exact same location as the comparative electrical strain gauges. Differences in readings obtained with the latter at different locations showed that the strains on the test surfaces were not identical.

The good results of the axial strain measurements are especially remarkable for the test with potash and limestone, where the surface images of the former were almost devoid of features and template matching series for both materials had relatively large standard deviations. It is also noteworthy that all results were obtained in spite of the large ratio between image displacements caused by the axial translation of the test specimens in the direction of the applied loads and the small displacements attributable to the compressional or dilative strains in the test specimen. In the experimental apparatus these translational displacements generally lead to difficulties in accurately determining the positions of the templates because of changes in lighting angles, image distortions and the movement of image features beyond the image boundaries.

In tests at 45° to the direction of the load it was found that most of the measurements with the optical sensor were to varying degrees erratic, which could be explained by the large axial translation of the test specimens relative to the small strain displacements obtained

at 45° . The results show that in the test with limestone there was good correlation while in the test with aluminum the optical sensor values follow the theoretical curve much closer than either of the electrical strain gauges. Poor correlation was obtained in tests with granite and potash.

Measurements with the optical sensor normal to the load were also to varying degrees erratic, again attributed to the large axial translation of the test specimens relative to the small strain displacements. In spite of this, the results of the optical strain gauge measurements were very good in the tests with aluminum and limestone. In the former, the data agree well with that of the theoretical strains and the measurements with one of the strain gauges. The optical strain gauge measurement in the test with granite followed the general trend of the electrical strain gauges but was slightly lower than the comparative values of the electrical strain gauges.

On the other hand, the test with potash was unstable at the low end of the load cycle while the remainder of the readings were stable but much higher than that of the electrical strain gauge. There was poor image quality in this test, which resulted in large deviations in the template matching sets that necessitated the elimination of a large number of values, particularly at the low load cycle. The cumulative displacement measurements may be influenced unfavorably when the first point of the curve is erroneous, which may have been the case in the test with potash.

As pointed out above, the experimental apparatus and test procedure had certain limitations which had a detrimental effect on the strain measurements. Particularly troublesome was the large axial translation of the test specimen. This translation is caused by: i) the relatively soft platform of the press used in the tests that flexes under load, especially at the low end of the load cycle, and ii) the contact effects between the platens and the specimen during load initiation. These effects do not come into play in field instrumentation and can be avoided or ameliorated in materials testing.

Another detrimental characteristic of the apparatus was the inability to obtain well focussed images. When placing one of the test samples under a regular microscope with the same magnification, it was possible to obtain an image which showed much better contrast than that obtained with the experimental apparatus. It should be possible to obtain similar quality images by optimizing the optical system. However, this was beyond the scope of the present work.

In general, the test series were successful in demonstrating the viability of the optical-digital strain sensor concept. There were discrepancies in some of the result, but as mentioned above, most of these can be attributed to some of the shortcomings in the experimental apparatus, the image processing method and the test procedures. The apparatus and procedures were not designed to optimize the optical-digital method, but merely to demonstrate the principle and to identify some of the characteristics of the method. In that, the test series has very well succeeded and has met its objectives.

CHAPTER 6: CONCLUSION AND RECOMMENDATIONS

The ultimate purpose of the experimental work was to validate the optical-digital method as a means to measure strains and to show that the method performs equally well or better than conventional methods, but with a major advantage that there is no need for contact with the surfaces to be measured.

In view of the successful results of the experimental work, in spite of all the shortcomings and limitations of the test apparatus, it is certain that an optimized system will result in an even more precise method with the potential of replacing many of the existing methods.

The use of a single, high resolution, camera with suitable optics for the creation of multi split images, and optimized coaxial lighting, would result in a very robust system which is insensitive to fluctuations, vibrations and positioning while still creating high quality images. The elimination of large displacements of the test specimen in materials testing would also lead to a significant augmentation of the method's accuracy. Research should be conducted to reduce or eliminate this effect. Finally, the template matching software is probably not the best method available. It is certain that research and development for the optimization of the image recognition & position determination will produce a more robust software which will be capable of producing more accurate results. Future work should involve the optimization of the system as discussed above.

Optimization and adaption of the novel method for the different applications will make it possible to match or surpass the performance of conventional strain measurements, however with the advantage that the sensor does not need contact with the surface. This has significant implications. It makes possible the conceptualization of novel rock mechanics instrumentation and the replacement of conventional methods, delivering measurements at a higher precision and accuracy and at a fraction of their cost. It also has applications in the domain of materials testing in general, and where strain measurements are not feasible (i.e. high temperature) in particular.

REFERENCES

Standard Test Method for Elastic Moduli of Intact Rock Core Specimens in Uniaxial Compression, Designation D 3148-86, 1989 Annual Book of ASTM Standards, Vol. 04.08 Section 4.

BASS J.D., et al (1986), Holographic In Situ Stress Measurements, Geophys. J. R. Astr. Soc. V.85, 14-41.

CHIANG F.P., et al (1980), Stress Analysis of In-Plane Vibration of 2-D Structures by a Laser Speckle Method, Applied Optics, V.19, No.16, 2705-2708.

COULOMBE A., CANTIN M. (1995), Rapport de la Phase II du projet: Appareil(s) de mesures sans contacts pour le Centre de Technologie Noranda, Solvision Inc.

DAS B.M. et al (1995), Brazilian Tensile Strength Test of Lightly Cemented Sand, Can. Geotech. J.; 32, 166-171.

DORNDORFER M.(1996), Video Extensometer ME-46, Messphysik Laborgraete Ges.m.b.H., Austria

DUK-WON PARK (1986), Holographic Testing Method of Rock, Proc.27th U.S Symposium on Rock Mechanics, 192-199.

FORURIA V. (1987), Borehole Slotting, A New In-Situ Method for Measuring Stresses in Hard Rock, Masters Thesis, James Cook University of North Queensland, Australia.

FRANKLIN J. (1990), Mine Monitoring Manual, The Canadian Institute of Mining and Metallurgy, Special Volume 42, 104-106.

GOODMAN R.E. (1980), Introduction to Rock Mechanics, John Wiley & Sons, New York, 181-183.

GREGORY D.A. (1979), Laser Speckle Photography and the Sub-Micron Measurement of Engineering Structures; NDT International, V.12 (2), 61-70.

JACOBY J.L., WILLIAMSON C.E. (1976), Optics Module for Borehole Stress Measuring Instrument, U.S. Patent 3,992,095.

JAEGGER AND COOK (1979), Fundamentals of Rock Mechanics, Chapman & Hall Ltd., London, 384-404.

JONES R. (1976), The Design and Application of a Speckle Pattern Interferometer for Total Plane Strain Field Measurement, Optics and Laser Technology, 215-218.

KANDUTH H., HUDYMA M. (1995), Method and Apparatus for Measuring Three Dimensional Stress in Rock Surrounding a Borehole; U.S. Patent No.5,381,690.

LEENDERTZ J.A. (1977), Speckle Pattern Interferometer, U.S. Patent 4,018,531.

LOTHIAN G.F. (1981), Optics and its Uses, Van Nostrand Reinhold Company, 182-183.

MARKS' STANDARD HANDBOOK FOR MECHANICAL ENGINEERS (1978), McGraw-Hill, ISBN 0-07-004123-7

PREATER R.W. (1980), Noncontact Method of In-Plane Strain Measurement on Rotating Structures, SPIE V.235, European Conference on Optical System Applications (Utrecht) 58-61.

RAMSEY S.D.Jr. (1974), Real Time Interferometry, U.S. Patent 3,828,126.

SICA L.Jr., HWALING H.S. (1981), Phase-Conjugate Interferometer, U.S. Patent 4,280,764.

SMITHER C.L. et al (1988), Analysis and Modelling of Holographic Measurements of In Situ Stress, Int.J.Rock Mech. Min. Sci. & Geomech. Abstr. V.25, No.6, 353-362.

VACHON R.I. (1986, 1991), Apparatus and Method for Determining Stress and Strain in Pipes, Pressure Vessels, Structural Members and Other Deformable Bodies, U.S.Patent 4,591,996 and U.S.Patent 5,065,331.